

# Efficiency Investigation of Line Start Synchronous Reluctance Motors

Motor Simulation and Testing with Respect to Induction Machine for Industrial Application

Master's thesis in Electric Power Engineering

Anton Kersten



MASTER'S THESIS 2017

# Efficiency Investigation of Line Start Synchronous Reluctance Motors

Motor Simulation and Testing with Respect  
to Induction Machine for Industrial Application

Anton Kersten



**CHALMERS**  
UNIVERSITY OF TECHNOLOGY

Department of Energy and Environment  
*Division of Electric Power Engineering*  
CHALMERS UNIVERSITY OF TECHNOLOGY  
Gothenburg, Sweden 2017

Efficiency Investigation of Line  
Start Synchronous Reluctance Motors  
Motor Simulation and Testing with Respect  
to Induction Machine for Industrial Application  
Anton Kersten

© Anton Kersten, 2017.

Supervisor: M.Sc. Daniel Pehrman, Department of Energy and Environment  
Examiner: Professor Dr. Yujing Liu, Department of Energy and Environment

Master's Thesis 2017  
Department of Energy and Environment  
Division of Electric Power Engineering  
Chalmers University of Technology  
SE-412 96 Gothenburg  
Telephone +46 31 772 1000

Cover: Illustration of the reluctance torque acting on an anisotropic shaped iron object within a magnetic field, while the isotropic object keeps being unaffected.

# Efficiency Investigation of Line Start Synchronous Reluctance Motors

Motor Simulation and Testing with Respect  
to Induction Machine for Industrial Application

Anton Kersten

Department of Energy and Environment  
Chalmers University of Technology

## **Abstract**

The need to constrain global warming demands new sustainable and green technologies. Line start synchronous reluctance machine technologies offer a big potential for future energy savings in industrial applications. Within this thesis the efficiency and starting capability of a novel line start synchronous reluctance machine in comparison to a common induction machine is analysed. For this purpose a simulation model and a test bench setup were used. With this new motor design a measured efficiency enhancement at rated load from 89.3% up to 92.0% was achieved, corresponding to a loss reduction of about 27.6%. For the chosen 4 kW four pole motor the efficiency rating was improved from IE3 to IE4. Nevertheless a drawback is the low synchronization capability, which limits the range of possible industry applications.

Keywords: synchronous reluctance motor, line start, direct on-line, induction machine, synchronization capability, efficiency enhancement.



## Acknowledgements

First of all I would like to thank my examiner Professor Dr. Yujing Liu for his guidance and support within this project and as my teacher. Additionally I would like to thank my supervisor Daniel Pehrman for his assistance and support, which made this thesis a great success. Further I would like to express sincere gratitude to Chalmers University of Technology, especially the staff of the division of Electric Power Engineering, who helped me always with proper advice and supported me on my career trajectory.

Anton Kersten, Gothenburg, May 2017



# Contents

<b>List of Figures</b>	<b>xi</b>
<b>List of Tables</b>	<b>xiii</b>
<b>Nomenclature</b>	<b>xv</b>
<b>1 Introduction</b>	<b>1</b>
1.1 Background . . . . .	1
1.2 Efficiency Classes and Regulations . . . . .	1
1.3 Feasibility Study . . . . .	2
1.4 Aim . . . . .	3
1.5 Problem Description . . . . .	3
1.6 Thesis Structure . . . . .	3
<b>2 Synchronous Reluctance Motor Theory</b>	<b>5</b>
2.1 Basic Reluctance Concept . . . . .	5
2.2 Synchronous Reluctance Machine . . . . .	8
2.3 Line Start Synchronous Reluctance Machine . . . . .	13
2.4 Synchronization Process . . . . .	17
<b>3 Line Start Machine Design</b>	<b>19</b>
<b>4 Simulation Model and Test Setup</b>	<b>23</b>
4.1 Simulation Model . . . . .	23
4.1.1 Solver Setting . . . . .	23
4.1.2 Meshing . . . . .	23
4.1.3 Efficiency and Power Factor Calculation . . . . .	24
4.2 Test Setup . . . . .	26
4.2.1 Testbench . . . . .	27
4.2.2 Measurements and Control . . . . .	28
4.2.3 Implementation in LabView . . . . .	30
4.2.4 Efficiency and Power Factor Calculation . . . . .	31
<b>5 Measurement and Simulation Results</b>	<b>33</b>
5.1 Test Bench and Setup Parameters . . . . .	33
5.2 Steady State Temperature . . . . .	34
5.3 Efficiency and Power Factor . . . . .	36

5.4	Inertia . . . . .	38
5.5	Synchronization Capability . . . . .	40
5.5.1	Start Capability - IM . . . . .	40
5.5.2	Synchronization Capability - LS-SynRM . . . . .	41
<b>6</b>	<b>Conclusion</b>	<b>45</b>
<b>7</b>	<b>Discussion and Future Work</b>	<b>47</b>
7.1	Sustainability and Ethical Aspects . . . . .	47
7.1.1	Rare Earth Materials . . . . .	48
	<b>Bibliography</b>	<b>49</b>

# List of Figures

1.1	Efficiency classes in dependance of motor rating. . . . .	2
2.1	Illustration of the reluctance torque acting on an anisotropic shaped iron object within a magnetic field, while the isotropic object keeps being unaffected. . . . .	5
2.2	Flux density and magnetic field distribution for a round shaped iron object when placed within a magnetic field for different orientations. . . . .	6
2.3	Flux density and magnetic field distribution for a rectangular shaped iron object when placed within a magnetic field for different orientations. . . . .	6
2.4	Inductance(a) and torque(b) for the two iron shapes with respect to the displacement angle $\delta$ . . . . .	7
2.5	Example of a four pole synchronous reluctance rotor with emphasized d- and q-axis . . . . .	9
2.6	Equivalent circuit of the SynRM in dq-components without iron losses. . . . .	10
2.7	Phasor diagram of the SynRM. . . . .	11
2.8	Reluctance torque in p.u. for different stator resistances in p.u.. . . . .	12
2.9	Equivalent circuit of the line start SynRM in dq-components. . . . .	13
2.10	Cage torque of LS-SynRM for different slips. . . . .	16
2.11	Starting process for different loadings resulting in a failed and a successful synchronization . . . . .	17
3.1	Induction (a) and synchronous reluctance(b) machine design for the four pole motor with 4kW rated output power. . . . .	20
3.2	Rotor shape with barrier cut-offs. . . . .	21
3.3	Line start SynRM rotors with aluminium(left) and copper(right) cage. . . . .	21
4.1	Mesh of the IM(a) and line start SynRM(b). . . . .	24
4.2	Schematic diagram of test setup including test motor M1 and DC machine M2. . . . .	26
4.3	Motor test bench including test and load motor. . . . .	27
4.4	Motor test bench with reduced inertia. . . . .	27
4.5	Placement and fixture of the temperature sensors in the end winding region. . . . .	28
4.6	Test setup including both motors and torque sensor. . . . .	29
4.7	Connection desk of the electrical setup. . . . .	29

4.8	Control desk of the test setup. . . . .	30
4.9	Schematic diagram of implemented LabView program. . . . .	31
5.1	Stator winding temperature rise for the three test machines when running on rated load. . . . .	34
5.2	Mean stator winding temperature for different loadings measured and approximated. . . . .	35
5.3	Efficiency simulation and measurement results for all three machines for different loadings. . . . .	36
5.4	Power factor simulation and measurement results for all three machines for different loadings. . . . .	37
5.5	Current(a) and Speed(b) for the different setups with respect to the displacement angle $\delta$ . . . . .	38
5.6	Speed(a) and torque(b) during the start up of the IM, if rated load is applied. . . . .	40
5.7	Reluctance torque at steady state(a) and cage torque at different slip speeds(b) . . . . .	41
5.8	Synchronization capability measurement for the SynRM-Al. . . . .	42
5.9	Synchronization capability measurement for the SynRM-Cu. . . . .	43
5.10	Synchronization capability of the SR machines. . . . .	44

# List of Tables

5.1	Viscous damping constant $B$ . . . . .	33
5.2	Motor efficiency for different loading. . . . .	36
5.3	Motor power factor for different loading. . . . .	37
5.4	System inertia with torque sensor. . . . .	39
5.5	System inertia without torque sensor. . . . .	39
5.6	Inertia of the machines' rotors. . . . .	39



# Nomenclature

## Abbreviations

DOL-SynRM	Direct On-Line Synchronous Reluctance Machine
FEM	Finite Element Method
IEC	International Electrotechnical Commission
IM	Induction Machine
IPF	Internal Power Factor
IPM	Interior Permanent Magnet Machine
LS-SynRM	Line Start Synchronous Reluctance Machine
MMF	Magneto Motive Force
PF	Power Factor
PMSM	Permanent Magnet Synchronous Machine
SR	Synchronous Reluctance
SynRM	Synchronous Reluctance Machine
SynRM-Al	Line Start Synchronous Reluctance Machine with Aluminium Cage
SynRM-Cu	Line Start Synchronous Reluctance Machine with Copper Cage



# 1

## Introduction

### 1.1 Background

To reduce exhaust fumes like  $CO_2$  emissions and constrain global warming, natural resources need to be used conscientiously and thoughtfully [1]. The worldwide energy consumption of electrical motors corresponds to about 40 % of the entire electrical energy production, while the average efficiency is about 88 % [2]. Increasing the efficiency of the used motors would lead to a decreased energy consumption and following to less emissions. The most used motor type within the field of industry applications is the induction machine. Its direct start ability makes it possible to run without an inverter. Furthermore the IM has a high robustness, whereby it can cope with sudden load changes easily. A common approach to improve the efficiency of an induction machine is an increased dimensioning to reduce ohmic losses in the stator windings and rotor bars. By this approach the machine often becomes large and bulky. Another opportunity to achieve a higher efficiency for the same dimensions, without using permanent magnets, could be a change using a different motor technology like a synchronous reluctance machine. Therefore a replacement of the IM's rotor by a synchronous reluctance rotor, which is additionally equipped with a squirrel cage, was proposed in a previous study project. Thereby the machine is capable to be started directly connected to the grid, rotor losses are decreased when reaching synchronous speed and following the steady state efficiency is improved. This type of machine is often referenced as line start or direct on line synchronous reluctance machine, abbreviated DOL-SynRM or LS-SynRM, respectively.

### 1.2 Efficiency Classes and Regulations

As a common interest of society the usage of more efficient motors for industry applications is regulated in many countries. Therefor motors are categorized into different efficiency classes. For example the IEC standard 60034-30-1 is a measure that classifies motors from IE1 to IE4, referred as classes Standard Efficiency to Super Premium Efficiency, respectively. Figure 1.1 depicts the efficiency class ratings for different rated motor output power. Within the frame of this thesis work a rated motor output power of 4kW is considered, emphasized in the graphic by a dashed line. Referring to this IEC standard, the European Parliament tries to regulate the use of efficient electrical motors in industrial environments to reduce the electrical energy consumption. Thus the directive 640/2009 and the supplement 04/2014 describe the energy usage and efficiency class regulation within the countries

belonging to the European Union[3][4]. Since January 2017 an efficiency rating of IE3 should be maintained for all motors directly connected to the grid with a rated output power of 1 to 100 kW [4]. The future trend shows a regulation for the usage of even more efficient motors, since it is discussed to introduce an IE5 rating over IE4, referenced as Gold Standard efficiency. The actual problem occurring for the customer, when replacing an old motor with a low efficiency rating due to a breakdown, is the increased dimension of the new motor system. This additional needed space can lead to further unintended adaptations in the work environment of the motor or in the worst case a replacement becomes even unfeasible.

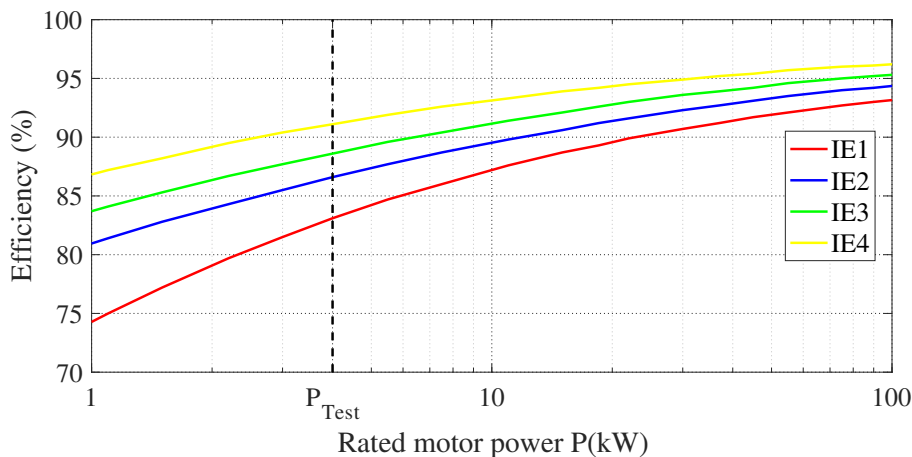


**Figure 1.1:** Efficiency classes in dependance of motor rating.

### 1.3 Feasibility Study

Within the frame of a previous study project a DOL synchronous reluctance machine was modeled and first simulations were performed in the FEM software ANSYS Maxwell. An induction machine with a 4kW power rating, an efficiency class IE3 and a frame size of 112 was chosen as a benchmark product. This selection was done in accordance to the already available DC load machine. Furthermore this type of machine is found quite often in industrial applications like conveyor belts, fans or pumps. Additionally there are various vendors worldwide. Within the study project the IM's stator and rotor were modeled to reach the performance values like efficiency and power factor in accordance to the data sheet. Subsequently the stator of the model was kept in the design model and the rotor was replaced by a synchronous reluctance rotor with small damper windings. The geometrical rotor parameters and the squirrel cage design were optimized to achieve a high efficiency. Hereby a potential for an efficiency improvement by one efficiency class was seen. Finally two SynRM prototypes, using a copper and an aluminum cage, were manufactured by the Swedish company BEVI Motors. The benchmark IM was also bought from the same company.

## 1.4 Aim

The efficiency enhancement of the 4 kW DOL synchronous reluctance machine compared to the benchmark induction machine with similar outer stator dimensions should be verified. Hereby the used design and simulation model should be assessed regarding its compliance with the obtained measurements. It should be shown, if the rotor adaption of the machine could result in a higher IE efficiency rating without changing the outer dimensions of the machine. Furthermore the starting capability of the synchronous reluctance machines should be determined for different loadings.

## 1.5 Problem Description

The efficiency values and starting capability of the motors need to be determined using actual measurements and simulations. Finally the results should be compared to the simulation model to verify it.

The project can be divided into the following sub tasks.

1. A reasonable test setup should be built allowing a controllable loading of the the AC motors.
2. Load tests and simulations should be performed to determine the machines' efficiencies and starting capabilities.
3. Simulated and actual results of the synchronous reluctance and induction machines should be compared and assessed critically. Hereby the simulation model should be verified.

The lab environment to test the motors should be set up. A DC machine should be used as a controllable load for the test motors. The needed voltage, current, torque, speed and temperature sensors should be implemented and a measurement acquisition system should be programmed. Hereby the sensors should be chosen to measure the electrical input power and the mechanical output power as accurate as possible to lead to a proper efficiency measurement.

Following, different tests should be performed measuring the motors' efficiencies and starting capabilities for different loadings.

The obtained results should be used to improve the simulation model regarding the steady state winding temperature and the system's inertia. Following, the simulated results should then be compared with the actual results. Finally the machines' efficiencies and starting performances should be assessed.

## 1.6 Thesis Structure

The structure of this thesis report is divided into 7 chapters including the introduction. The second chapter covers the basic principles of the synchronous reluctance machine theory and the line start concept to reach synchronization. Following, a brief description of the prior designed line start reluctance machine is given. The fourth chapter gives an overview about the FEM machine simulation models and a brief description of the lab setup for the actual machines. The subsequent chapter presents the results from the performed simulations and measurements of the

machines, whereby those are assessed and compared . Subsequently a conclusion summarizing the main results. Finally the report gives a brief discussion and mentions possible future work tasks. Moreover the discussion includes a reflection on some sustainable and ethical aspects with a focus on the mining of rare earth materials. This aspect was chosen, because the efficiency enhancement of the deigned LS-SynRM was not achieved by harnessing permanent magnets.

# 2

## Synchronous Reluctance Motor Theory

The following chapter gives a description about the basic reluctance principle and the utilization in an electrical motor. Further the behavior of the SynRM, if a cage is added to the rotor of it to achieve a line start ability, is explained.

### 2.1 Basic Reluctance Concept

A reluctance machine is called like the utilized torque concept, which is illustrated in Figure 2.1. Here two different shaped iron objects are placed inside a magnetic field in air. The reluctance force tries to align the rectangular shaped iron object, while the round shaped object is unaffected [5]. This kind of principle is commonly known and it is for example utilized in a compass, where the metallic needle aligns with the magnetic field of the earth.

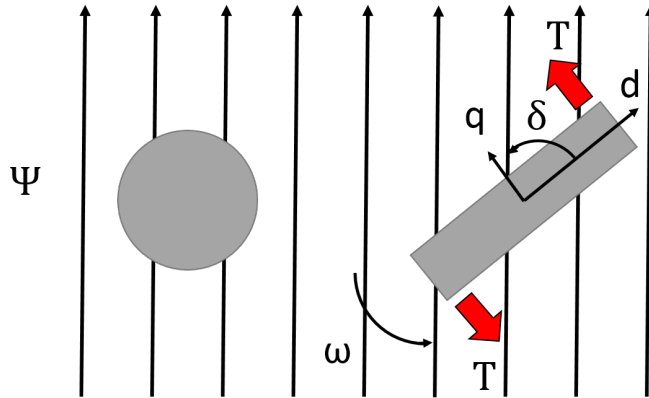


**Figure 2.1:** Illustration of the reluctance torque acting on an anisotropic shaped iron object within a magnetic field, while the isotropic object keeps being unaffected.

The reason for this alignment force can be explained starting by the relation between work and force. The general term for the physical work for a force along a certain distance can be described as in (2.1), which can be rewritten to (2.2). This shows that the torque  $T$  is caused by a change of the stored energy with respect to the angle  $\delta$ .

$$W = \int_{s_1}^{s_2} \vec{F} d\vec{s} = \int_{\delta_1}^{\delta_2} \vec{T} d\vec{\delta} \quad (2.1)$$

$$T = \frac{dW}{d\delta} \quad (2.2)$$

Following, the magnetic energy stored in an inductor can be determined by its inductance and the current or by the volume integral of the product of permeability and the square of the magnetic field quantity  $H$ , as described in (2.3).

$$W = \frac{1}{2}I^2L(\delta) = \frac{1}{2} \iiint_V BHdv = \frac{1}{2} \iiint_V \mu H^2 dv \quad (2.3)$$

Figures 2.2 and 2.3 depict the magnetic field distribution and the flux density in and around the two different shaped iron objects obtained from a FEM simulation in COMSOL Multiphysics.

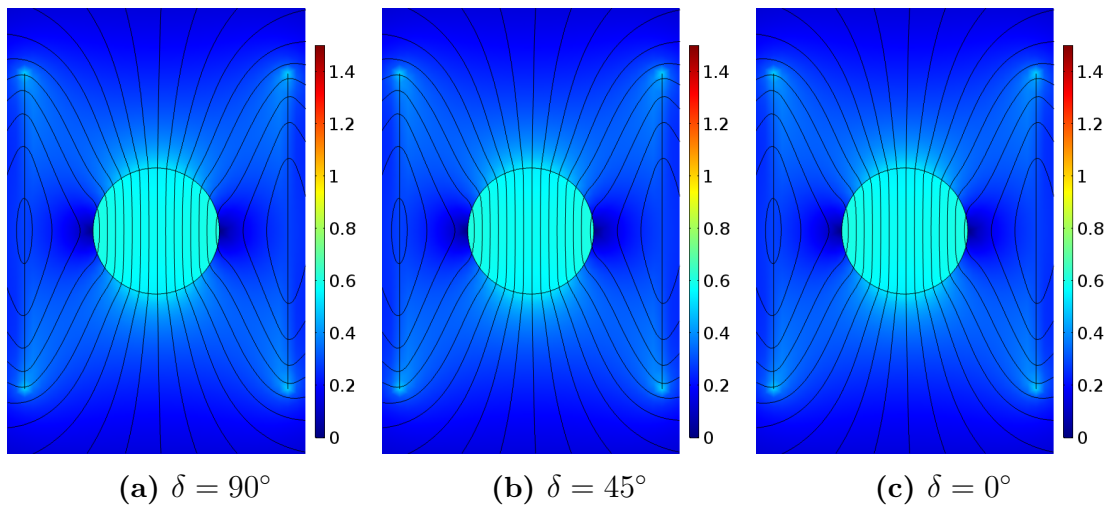


**Figure 2.2:** Flux density and magnetic field distribution for a round shaped iron object when placed within a magnetic field for different orientations.

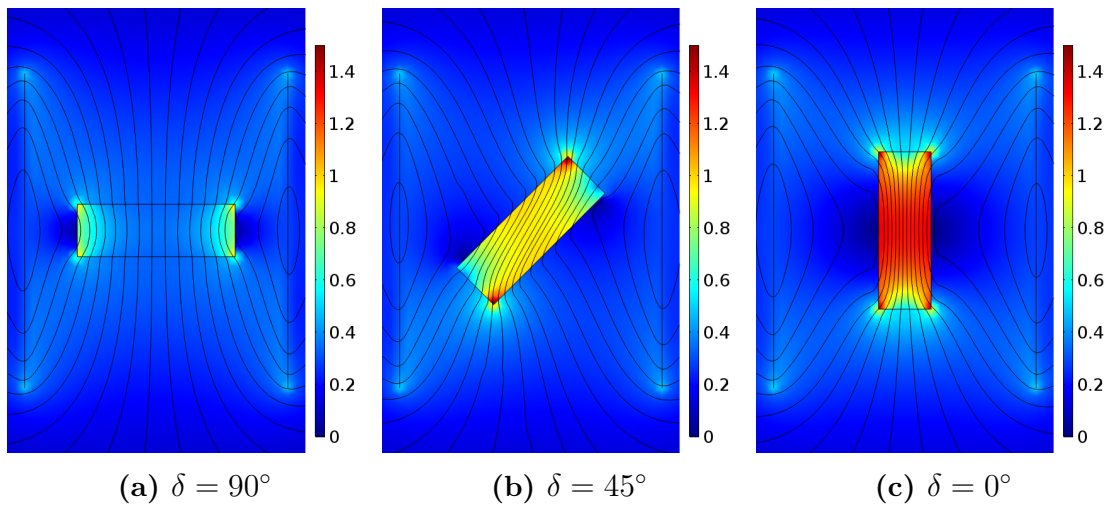


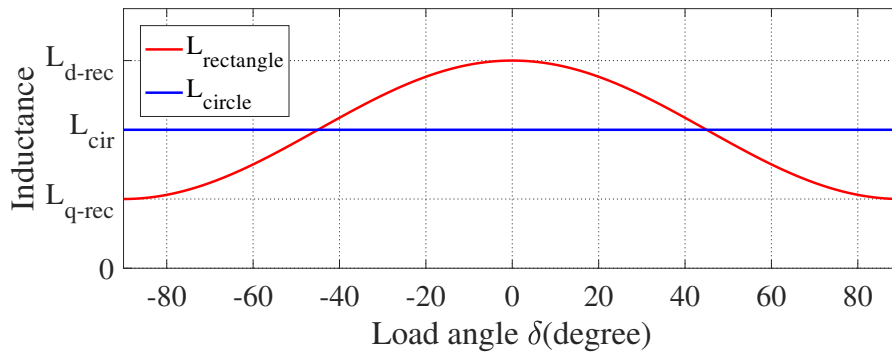
**Figure 2.3:** Flux density and magnetic field distribution for a rectangular shaped iron object when placed within a magnetic field for different orientations.

The objects are placed between two infinitely thin conductors, carrying a certain line current in opposite directions, whereby the created magnetic field is enhanced between the two conductors. Due to its high relative permeability the iron is a low reluctance path for the magnetic field and the flux is attracted to penetrate the objects resulting in a high flux density inside the iron. From Figure 2.2 it can be seen that the field distribution and the magnetic flux density are unaffected by the rotation of the round iron body. On the opposite, Figure 2.3 shows different flux distributions and flux densities dependent on the rotational angle  $\delta$ . Therefore the magnetic energy density as described in (2.4) can be used in the FEM software tool, like depicted in (2.5), to determine the inductance for different displacements. Computing the derivative of the energy leads subsequently to the torque dependency on  $\delta$ .

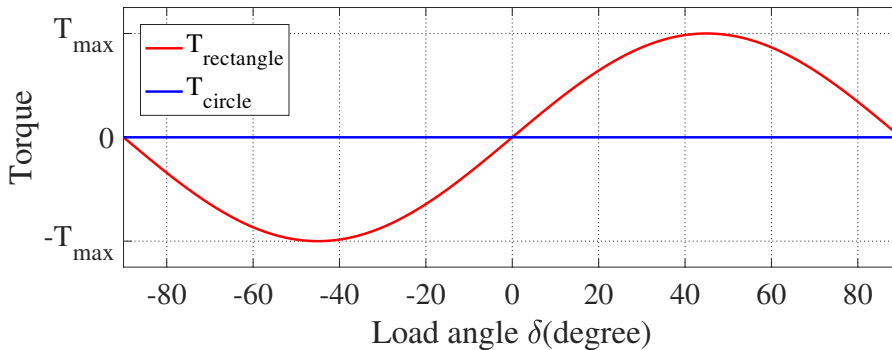
$$w_m = \frac{1}{2}BH = \frac{1}{2}\mu H^2 \quad (2.4)$$

$$L(\delta) = \iiint_V \frac{2w_m}{I^2} dv \quad (2.5)$$

Figure 2.4 shows the obtained inductance and torque values for different displacements. It can be seen that the inductance of the rectangular object follows a trigonometric function, whereas the circular shaped object's inductance is kept constant.



(a) Inductance



(b) Torque

**Figure 2.4:** Inductance(a) and torque(b) for the two iron shapes with respect to the displacement angle  $\delta$ .

These obtained inductances cause a sinusoidal and zero torque behaviour in respect of the displacement  $\delta$ , as seen in Figure 2.4b. Following the inductance of the rectangular object is determined to follow a shape as described in (2.6).

$$L(\delta) = \frac{L_d - L_q}{2} \cos(-2\delta) + \frac{L_d + L_q}{2} \quad (2.6)$$

Inserting (2.6) and (2.3) in (2.2) leads to (2.7), which in turn shows a sinusoidal torque production in respect of the angle  $\delta$ .

$$T = \frac{1}{2} I^2 \frac{L_d - L_q}{2} \sin(2\delta) \quad (2.7)$$

The conclusion can be drawn that the system always tends to achieve a state resulting in a minimal reluctance. The rectangular shaped object is experiencing a torque acting on it as long the d-axis is not aligned with the magnetic flux, whereas the depicted isotropic round shaped object's reluctance does not change when rotating in the magnetic field. Following there is no force acting on the round shaped object. The extent of the torque depends on the inductance ratio of the d- and q-axis and the load angle or rather called current angle  $\delta$ , defined as the angle between the magnetic field and the d-axis of the object. Changing the torque expression from (2.7) to (2.8), the torque can be expressed in dependence of the d- and q-current as in (2.9).

$$T = \frac{1}{2} (L_d - L_q) I^2 \sin(\delta) \cos(\delta) \quad (2.8)$$

$$T = \frac{1}{2} (L_d - L_q) i_d i_q \quad (2.9)$$

## 2.2 Synchronous Reluctance Machine

The most common types of reluctance machines are switched and synchronous reluctance motors. Within the frame of this thesis work it is dealt with a synchronous reluctance machine as part of a line start synchronous reluctance motor.

To apply the reluctance torque principle, described in the previous section, to an electrical machine, a rotating magnetic field and an anisotropic rotor shape are required. Therefore a common three phase induction machine stator producing a rotating MMF can be utilized and a replacement of the rotor is needed. Figure 2.5 depicts a 2-D design as an example of a typical 4-pole synchronous reluctance rotor shape. The q- and d-axis are emphasized. To achieve an anisotropic rotor shape the flux in the d-axis should experience a low reluctance, while the flux in q-axis is constrained by introduced air barriers and an optional cutoff at the rotor's edge. The maximum torque produced by the machine depends on the inductance difference, whereby a high torque can be exploited, if maximizing  $L_d$  and minimizing  $L_q$ . On the contrary the ratio of the inductance in d- and q-axis is called saliency ratio as seen in (2.10). Hereby the internal power factor  $IPF$  can be described as depicted in equation (2.11) [5].

$$\xi = \frac{L_d}{L_q} \quad (2.10)$$

$$IPF_{max} = \cos\phi = \frac{\xi - 1}{\xi + 1} \quad (2.11)$$

The number and size of barriers are chosen in a manner that a sinusoidal d-axis MMF in the air gap along the segments is achieved. A more detailed description about the design of synchronous reluctance rotors regarding torque, power and torque ripple optimization can be found in [5].

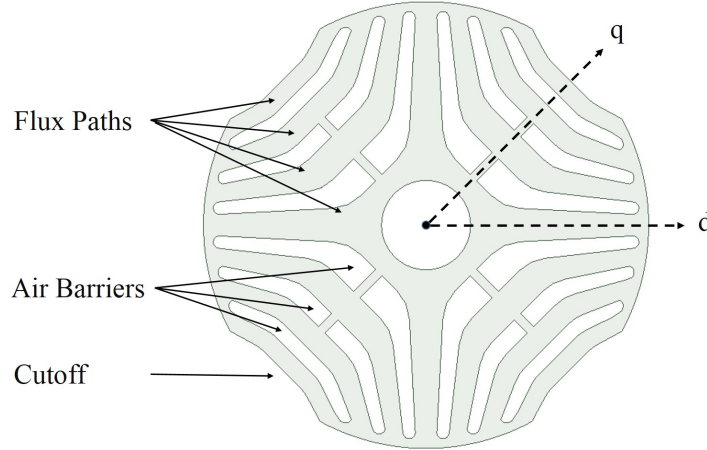


**Figure 2.5:** Example of a four pole synchronous reluctance rotor with emphasized d- and q-axis .

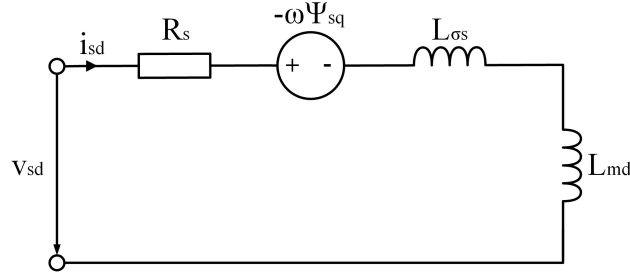
When using a three phase stator the torque expression needs to be adapted according to the number of pole pairs as seen in equation (2.12).

$$T_e = \frac{3 n_p}{2} (L_d - L_q) i_{ds} i_{qs} \quad (2.12)$$

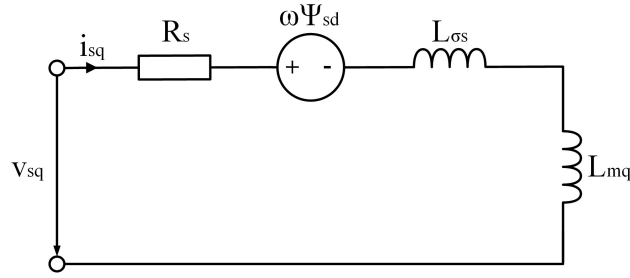
To produce a constant torque the rotor needs to revolve with the same speed as the mains divided by the number of pole pairs. For this reason the SynRM cannot be started directly connected to the grid. At synchronous speed the load torque is changing in respect to the angle between the stator flux and the d-axis of the rotor, often called torque, load or current angle  $\delta$ . If current control is used the torque curve looks similar as for a common synchronous machine.

The efficiency of a SynRM is usually higher than an induction machine's efficiency, assuming same outer dimensioning. Due to the absence of the squirrel cage the rotor losses are reduced. When running at synchronous speed the SynRM is able to handle load changes easily and it can cope with overloading up to a certain load angle without changing its efficiency significantly. The temperature in stator and especially in the rotor are reduced. Considering its mechanical construction it is robust and works without any brushes and commutators. One of its disadvantages is the reduced power factor compared to the induction machine. Another drawback is its non-start ability, if directly connected to the grid, due to the inertia of the rotor and the fast rotating magnetic field produced by the stator, similar like for PMSM,

IPM or separately excited synchronous machines [5]. The equivalent circuit of the SynRM in d- and q-reference can be seen in Figure 2.6 [5]. The stator resistance  $R_s$  and leakage inductance  $L_s$  are independent of the d- and q-reference. However the magnetizing inductances  $L_{md}$  and  $L_{mq}$  differ from each other, resulting also in different d- and q-flux linkages. Additionally there is a cross coupling effect of the back EMF, corresponding to the fluxes in d- and q-axis. The iron losses are not considered.



(a) d-reference



(b) q-reference

**Figure 2.6:** Equivalent circuit of the SynRM in dq-components without iron losses.

The equations (2.13) and (2.14) are the governing equations describing the electrical behaviour of the synchronous reluctance machine neglecting saturation. Hereby  $L_{sd}$  and  $L_{sq}$  can be written as  $L_{\sigma s} + L_{md}$  and  $L_{\sigma s} + L_{mq}$ , respectively.

$$\bar{v}_s = R_s \bar{i}_s + \frac{d\bar{\psi}_s}{dt} + j\omega_s \bar{\psi}_s \quad (2.13)$$

$$\bar{\psi}_s = L_{\sigma s} \bar{i}_s + \begin{bmatrix} L_{md} & 0 \\ 0 & L_{mq} \end{bmatrix} \bar{i}_s \quad (2.14)$$

A general term for the torque of a three phase machine is given in (2.15). Inserting the stator flux and current lead to (2.16). If current excitation is applied the torque can be expressed as in (2.17).

$$T_e = \frac{3n_p}{2} \text{Im}(\bar{\psi}_s^* \bar{i}_s) \quad (2.15)$$

$$T_e = \frac{3n_p}{2} (\psi_{sd} i_{sq} - \psi_{sq} i_{sd}) = \frac{3n_p}{2} (L_{sd} - L_{sq}) i_{sd} i_{sq} \quad (2.16)$$

$$T_e = \frac{3n_p}{2}(L_{sd} - L_{sq})I \sin(\delta_i) I \cos(\delta_i) = \frac{3n_p}{4}(L_{sd} - L_{sq})I^2 \sin(2\delta_i) \quad (2.17)$$

If voltage excitation is used the torque expression becomes different. Firstly the currents in (2.16) need to be expressed in dependence of the voltage. For this purpose the stator flux and voltage in dq-quantities at steady state can be rewritten to (2.18) and (2.19), respectively.

$$\begin{aligned} \bar{\psi}_{sd} &= L_{sd} \bar{I}_{sd} \\ \bar{\psi}_{sq} &= L_{sq} \bar{I}_{sq} \end{aligned} \quad (2.18)$$

$$\begin{bmatrix} \bar{V}_{sd} \\ \bar{V}_{sq} \end{bmatrix} = \begin{bmatrix} R_s & -\omega L_{sq} \\ \omega L_{sd} & R_s \end{bmatrix} \begin{bmatrix} \bar{I}_{sd} \\ \bar{I}_{sq} \end{bmatrix} \quad (2.19)$$

Solving (2.19) for the voltage vector by multiplying both sides of the matrix equation with the admittance matrix, the obtained dq-quantities of the current can be written as in (2.20). The reactances are written as  $X_d$  and  $X_q$ .

$$\begin{bmatrix} \bar{I}_{sd} \\ \bar{I}_{sq} \end{bmatrix} = \frac{1}{R_s^2 + X_d X_q} \begin{bmatrix} R_s & -X_d \\ X_q & R_s \end{bmatrix} \begin{bmatrix} \bar{V}_{sd} \\ \bar{V}_{sq} \end{bmatrix} \quad (2.20)$$

To express the voltage in dq-quantities the load or voltage angle  $\delta_v$  as the displacement between the voltage phasor and the q-axis as seen in Figure 2.7 is introduced [6]. The dq-quantities of the supply voltage can then be expressed as in (2.21).

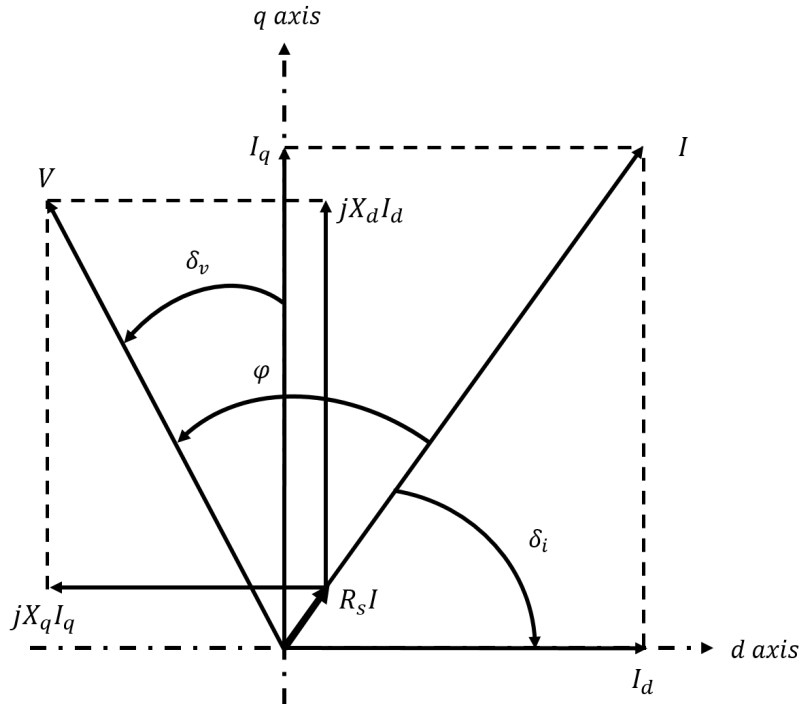


**Figure 2.7:** Phasor diagram of the SynRM.

$$\begin{aligned} V_{sd} &= -\hat{V} \sin(\delta_v) \\ V_{sq} &= +\hat{V} \cos(\delta_v) \end{aligned} \quad (2.21)$$

When inserting (2.21) in (2.19) the dq-stator current is obtained. Inserting the stator current in the torque equation (2.16) leads to the final torque expression for a voltage excited SynRM (2.22).

$$\begin{aligned} T_e &= \frac{3n_p}{2} \cdot \frac{V^2}{2} \cdot \frac{(L_{sd} - L_{sq})}{(R_s^2 + X_d X_q)^2} \cdot \{(X_d X_q - R_s^2) \sin(2\delta_v) \\ &\quad + R_s(X_q - X_d) - R_s(X_q + X_d) \cos(2\delta_v)\} \end{aligned} \quad (2.22)$$

The torque expression becomes the same as for a current excited machine, if the stator winding resistance  $R_s$  is zero. Figure 2.8 shows the reluctance torque for different stator resistances in p.u.. It can be seen that an increase in resistance decreases the pull-out torque and shifts the torque curve downwards. The torque curves are not point symmetrical anymore. Especially for small machines the influence of the stator resistance cannot be neglected and the torque curve cannot be approximated by a simple trigonometric function.

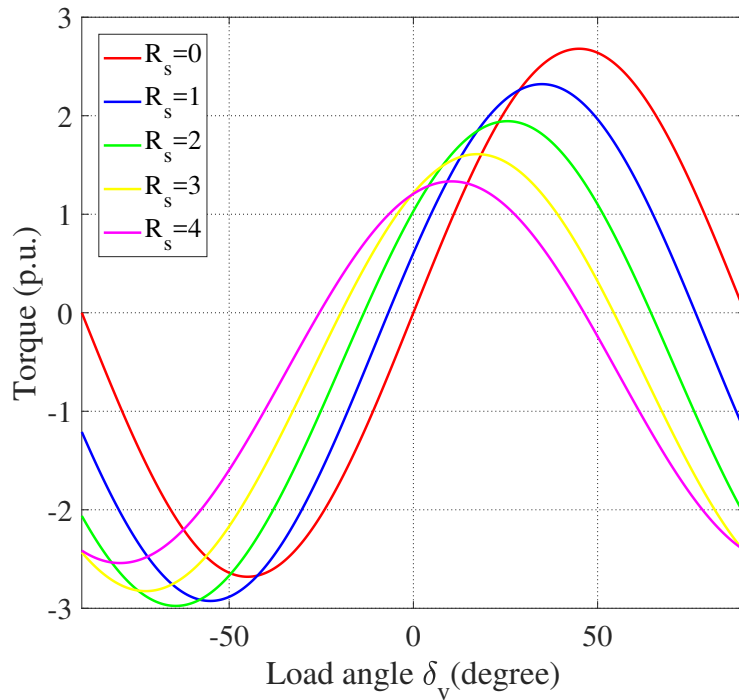


**Figure 2.8:** Reluctance torque in p.u. for different stator resistances in p.u..

### 2.3 Line Start Synchronous Reluctance Machine

To overcome the non-starting ability of a synchronous reluctance machine, a cage can be inserted in the air barriers of the reluctance rotor. Often the air barriers are just filled with a conductive material in a die cast process and the terminals of the cage are short circuited by a ring at each end. Commonly aluminum is used as the cage material. This cage introduces a positive torque component during start up and helps the machine to run into synchronism. If synchronism is reached there is basically no voltage in the cage induced, whereby the losses are decreased compared to an IM. The equivalent circuit of the line start SynRM in dq-quantities is depicted in Figure 2.9 [7].

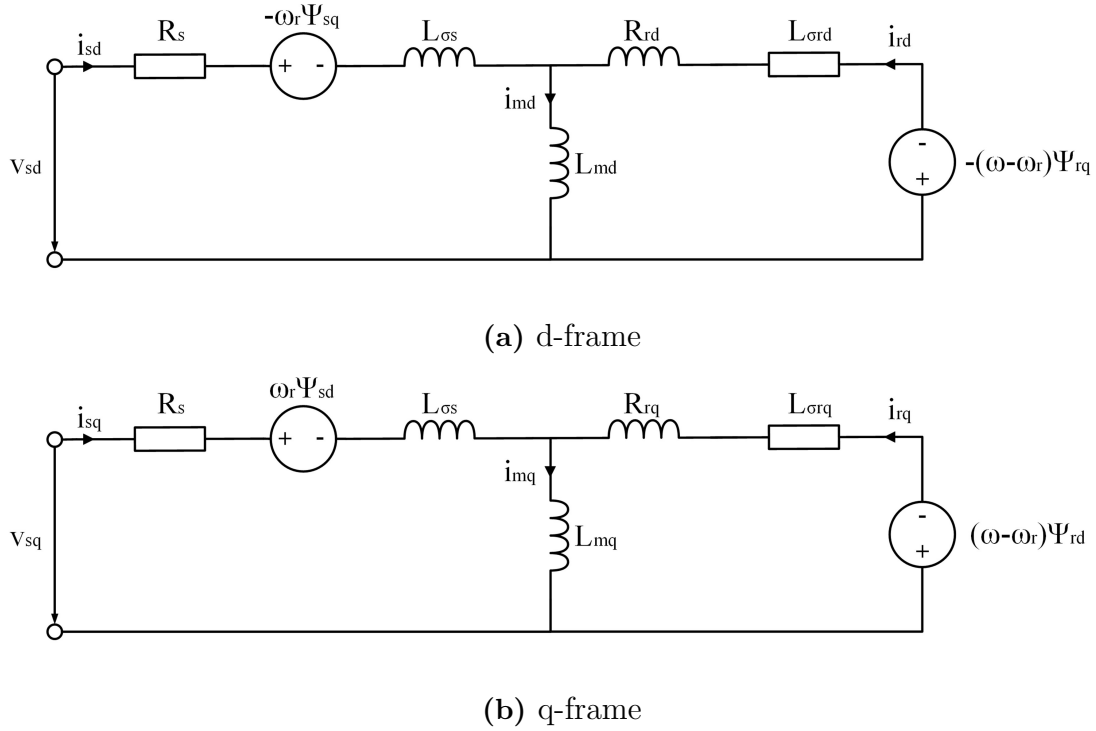


**Figure 2.9:** Equivalent circuit of the line start SynRM in dq-components.

The governing system equations (2.23) to (2.27) include additional rotor equations for the IM part of this hybrid machine.

$$\bar{v}_s = R_s \bar{i}_s + \frac{d\bar{\psi}_s}{dt} + j\omega_r \bar{\psi}_s \quad (2.23)$$

$$0 = \begin{bmatrix} R_{rd} & 0 \\ 0 & R_{rq} \end{bmatrix} \bar{i}_r + \frac{d\bar{\psi}_r}{dt} + j(\omega - \omega_r) \bar{\psi}_r \quad (2.24)$$

$$\bar{\psi}_s = L_{\sigma s} \bar{i}_s + \begin{bmatrix} L_{md} & 0 \\ 0 & L_{mq} \end{bmatrix} \bar{i}_m \quad (2.25)$$

$$\bar{\psi}_r = \begin{bmatrix} L_{\sigma rd} & 0 \\ 0 & L_{\sigma rq} \end{bmatrix} \bar{i}_r + \begin{bmatrix} L_{md} & 0 \\ 0 & L_{mq} \end{bmatrix} \bar{i}_m \quad (2.26)$$

## 2. Synchronous Reluctance Motor Theory

---

$$\bar{i}_m = \bar{i}_s + \bar{i}_r \quad (2.27)$$

The electrical torque during start up becomes a compound of the cage and the oscillating reluctance torque as seen in (2.28).

$$T_e = \frac{3n_p}{2} \text{Im}(\bar{\psi}_s^* \bar{i}_s) = T_{cage} + T_{rel} \quad (2.28)$$

To determine the cage and reluctance torque [7] of the machine while running up for different slip speeds  $s$ , the system equations can be written as in (2.29) and (2.30). It is assumed that the electrical transient is way faster than the mechanical transient. Consequently in steady state the time derivatives can be replaced by  $j(sw)$ , which is valid for sinusoidal phasors. The angular velocity of the phasors is  $sw$  using the rotor frame as the reference.

$$\begin{aligned} V_{sd} &= R_s I_{sd} + j s \omega \psi_{sd} - \omega_r \psi_{sq} \\ V_{sq} &= R_s I_{sq} + j s \omega \psi_{sq} + \omega_r \psi_{sd} \end{aligned} \quad (2.29)$$

$$\begin{aligned} 0 &= R_e I_{rd} + j s \omega \psi_{rd} \\ 0 &= R_e I_{rq} + j s \omega \psi_{rq} \end{aligned} \quad (2.30)$$

To eliminate the rotor currents from (2.30), these can be expressed using the current divider rule resulting in (2.31).

$$\begin{aligned} I_{rd} &= \frac{j s \omega L_{md}}{R_{rd} + j s \omega L_{rd}} I_{sd} \\ I_{rq} &= \frac{j s \omega L_{mq}}{R_{rq} + j s \omega L_{rq}} I_{sq} \end{aligned} \quad (2.31)$$

Consequently the stator flux can be written like in (2.32). Here the terms  $\bar{Z}_{pd}$  and  $\bar{Z}_{pq}$  are called operational impedances.

$$\begin{aligned} \bar{\psi}_{sd} &= \left( L_{sd} - \frac{j s \omega L_{md}^2}{R_{rd} + j s \omega L_{rd}} \right) \bar{I}_{sd} = \bar{Z}_{pd} \bar{I}_{sd} \\ \bar{\psi}_{sq} &= \left( L_{sq} - \frac{j s \omega L_{mq}^2}{R_{rq} + j s \omega L_{rq}} \right) \bar{I}_{sq} = \bar{Z}_{pq} \bar{I}_{sq} \end{aligned} \quad (2.32)$$

The relation of voltage and current can be written as in (2.33), which needs to be solved for the stator current by multiplying both sides with the admittance matrix. Through this equation (2.36) is obtained, whereby  $D_c$  is stated in (2.37).

$$\begin{bmatrix} \bar{V}_{sd} \\ \bar{V}_{sq} \end{bmatrix} = \begin{bmatrix} (R_s + j s \omega \bar{Z}_{pd}) & -(1-s)\omega \bar{Z}_{pq} \\ (1-s)\omega \bar{Z}_{pq} & (R_s + j s \omega \bar{Z}_{pq}) \end{bmatrix} \begin{bmatrix} \bar{I}_{sd} \\ \bar{I}_{sq} \end{bmatrix} \quad (2.33)$$

The stator voltage can be written as in (2.34). If the slip is not zero, the voltage quantities become rotating phasors in the dq-frame. Therefore the voltage for  $s \neq 0$  can be written as (2.35), whereby  $\delta_v$  can be neglected.

$$\begin{aligned} V_{sd} &= -\hat{V} \sin(s\omega t + \delta_v) \\ V_{sq} &= +\hat{V} \cos(s\omega t + \delta_v) \end{aligned} \quad (2.34)$$

$$\begin{aligned} V_{sd} &= j\hat{V} \\ V_{sq} &= \hat{V} \end{aligned} \quad (2.35)$$

$$\begin{bmatrix} I_{sd} \\ I_{sq} \end{bmatrix} = \frac{1}{D_c} \begin{bmatrix} (R_s + js\omega\bar{Z}_{pq}) & (1-s)\omega\bar{Z}_{pq} \\ -(1-s)\omega\bar{Z}_{pd} & (R_s + js\omega\bar{Z}_{pd}) \end{bmatrix} \begin{bmatrix} j\hat{V} \\ \hat{V} \end{bmatrix} \quad (2.36)$$

$$D_c = R_s^2 + js\omega R_s(\bar{Z}_{pd} + \bar{Z}_{pq}) + (1-2s)\omega^2 \bar{Z}_{pd}\bar{Z}_{pq} \quad (2.37)$$

Nevertheless it is cumbersome to obtain an analytical expression, which can be handled, for the currents and flux. Therefore the real and imaginary part of stator current and flux are substituted by variables, which leads to (2.38), which in turn can be used to compute the torque recalling (2.15).

$$\begin{aligned} I_{sd} &= a + jb \\ I_{sq} &= c + jd \\ \psi_{sd} &= e + jf \\ \psi_{sq} &= g + jh \end{aligned} \quad (2.38)$$

From [7] the cage and reluctance torque contribution can be calculated according to the equations (2.39) to (2.42). The cage torque is a constant value for different slip values. The cage is supposed to accelerate the machine's speed to asynchronous speed as close to synchronous speed as possible. On the other side it can be seen that the reluctance torque contribution is a trigonometric function oscillating with twice the slip frequency. The amplitude is also depending on the slip.

$$T_e = T_{cage} + \hat{T}_{rel} \cdot \sin(2s\omega t - \alpha) \quad (2.39)$$

$$T_{cage} = \frac{3n_p}{4} \cdot (ce + df - ga - bh) \quad (2.40)$$

$$\hat{T}_{rel} = \frac{3n_p}{4} \sqrt{(ce + bh - df - ga)^2 + (ed + cf - gb - ah)^2} \quad (2.41)$$

$$\alpha = \arctan \left( \frac{gb + ah - ed - cf}{ce + bh - df - ga} \right) \quad (2.42)$$

The contribution of the cage torque for different rotor resistances is plotted in Figure 2.10. For symmetrical rotor resistances the torque speed curves have the same shape as a typical induction machine, except that there is a negative contribution around zero slip, which is typical for a voltage excited reluctance machine with a big stator resistance [6]. When introducing a rotor resistance that is higher in d-reference than in q-reference or vice versa, the torque curves get distorted especially around half speed and throughout the subsynchronous slip region. This phenomenon, referenced as Georges phenomenon, is known from induction machines with an unbalanced rotor [8]. However the utilization of the reluctance torque requires unsymmetrical magnetizing inductances, which in turn hinder the design of a symmetrical rotor resistance.

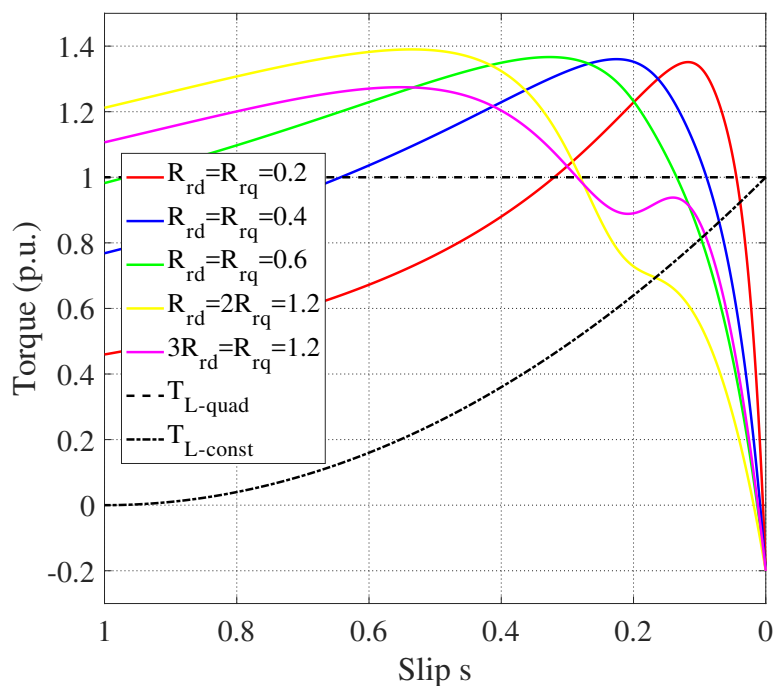
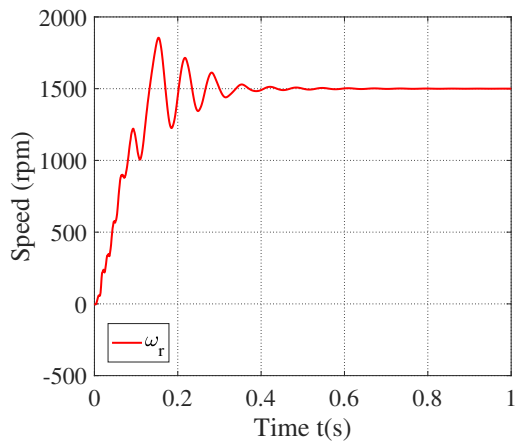


**Figure 2.10:** Cage torque of LS-SynRM for different slips.

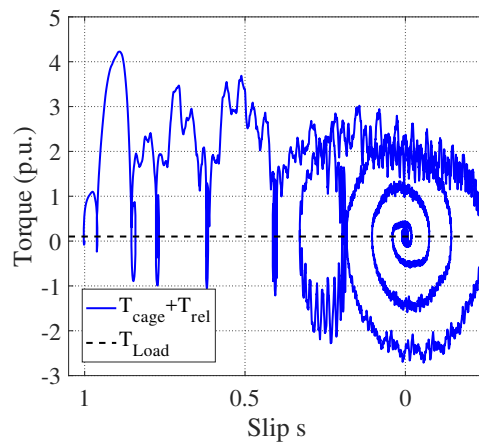
After a successful run up and synchronization, the contribution of the cage torque extinguishes. Following the torque equation at synchronous speed at steady state becomes the same as described in (2.22).

## 2.4 Synchronization Process

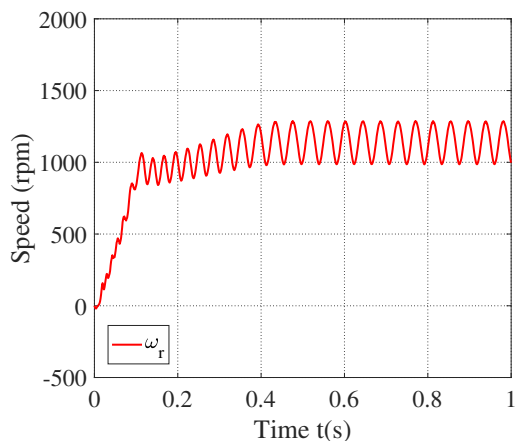
Figure 2.11 depicts the speed over time and the electrical torque over slip for two start scenarios with different loadings of 10% and 50% referred to the rated load, for a successful and failed synchronization process, respectively. In the transients shown in Figure 2.11a and Figure 2.11b, it can be seen how the speed exceeds the synchronous speed of 1500 rpm quickly and gets damped into synchronous speed at around 0.5s. The torque slip plot shows how the torque, as a compound of the reluctance and cage torque, is varying in the beginning until the intersection of the load torque with the electrical torque is reached. The synchronization attempt starts subsequently and the slip becomes even negative. Following, the oscillations are damped and the torque equilibrium is reached. Figures 2.11c and 2.11d depict a failed synchronization process.



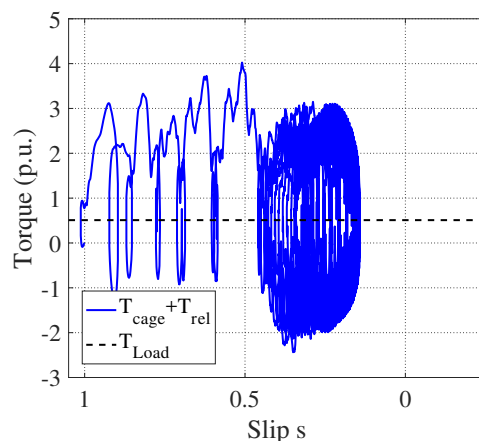
(a) Speed successful synchronization



(b) Torque successful synchronization



(c) Speed failed synchronization



(d) Torque failed synchronization

**Figure 2.11:** Starting process for different loadings resulting in a failed and a successful synchronization

It can be seen that the speed ends up at an oscillating pseudo steady state with a big slip. Hereby the high rotor losses can destroy the rotor bars of the machine. Further

the torque slip plot shows a similar behaviour as before, though the system's energy is not sufficient to reach zero slip, resulting in an infinite loop of synchronization attempts. To find an accurate analytical criteria for the prediction of a successful synchronization is quite difficult. One method is described in [9] and [10], in which the torque equations are simplified and the initial conditions are approximated.

In general the mechanical equation of the system can be written as (2.43), where the electrical torque is expressed as in (2.44).

$$J \frac{d\omega}{dt} = T_e - T_l \quad (2.43)$$

$$T_e = T_{rel}(\delta) + T_{cage} \left( \frac{d\delta}{dt} \right) \quad (2.44)$$

The energy stored in a rotating mass can be calculated using (2.45), whereby the energy at synchronous speed and slip speed can be calculated as (2.46) and (2.47), respectively.

$$E = \frac{1}{2} J \omega^2 \quad (2.45)$$

$$E_1 = \frac{1}{2} J \omega_s^2 \quad (2.46)$$

$$E_2 = \frac{1}{2} J \omega_s^2 (1 - s_0)^2 \quad (2.47)$$

So the energy needed to lift the system's speed of an inertia  $J$  to synchronous speed can be calculated by the energy difference as described in (2.48).

$$E_{sync} = E_1 - E_2 = \frac{1}{2} J \omega_s^2 (1 - (1 - s_0)^2) \quad (2.48)$$

For further investigations it is assumed that the critical synchronisation point occurs, if the system does not exceed the synchronous speed, meaning the slip  $s$  becomes zero[9]. The maximum electrical system energy contributing to the synchronisation can be expressed as followed in (2.49).

$$E_{system} = \int_{\delta_{start}}^{\delta_{crit}} T_{rel}(\delta) d\delta + \int_{\delta_{start}}^{\delta_{crit}} T_{cage} \left( \frac{d\delta}{dt} \right) d\delta + \int_{\delta_{start}}^{\delta_{crit}} T_l d\delta \quad (2.49)$$

To achieve a successful synchronization the available system energy must be greater than the needed synchronization energy as stated in (2.50).

$$E_{system} \geq \frac{1}{2} J \omega_s^2 (1 - (1 - s_0)^2) \quad (2.50)$$

The problem of this method is that the initial conditions of the synchronisation regarding slip  $s$  and the load angle are not known. Further the reluctance pull out-torque is also slip dependent. Nevertheless it can be seen that the inertia and asynchronous slip are a measure to determine the needed synchronization energy, whereas the available pull-in energy depends on the reluctance, cage and load torque.

# 3

## Line Start Machine Design

Within this chapter a brief introduction of the prior designed line start synchronous reluctance machine is given. Hereby the main focus of the design was the proper placement of the rotor cage bars and additional measures resulting in a high steady state efficiency.

Figures 3.1a and 3.1b show the cross-section of the IM benchmark motor and the designed line start synchronous reluctance machine, respectively. Due to symmetrical reasons just a quarter of the four pole machines is depicted. For both machines the same stator is used.

The benchmark motor was chosen to have a rated efficiency of 88.6 % (IE3), power factor of 0.79 and a mechanical output power of 4 kW with 400 V phase voltage, while the machines' windings are connected in delta.

For the design and the simulations of the line start synchronous reluctance machine the FEM software ANSYS Maxwell is used, in which a 2D one layer design model topology without thermal coupling was chosen. Thereby an acceptable trade-off between a short computation time and accurate simulation results for different parametric sweep studies was achieved. For simplicity the steady state temperature of the rotor bars and stator windings were set to an equal value. During the design stage it was assumed that the steady state temperature would reach around 50 % of the temperature rise of the corresponding insulation class F. Assuming an ambient temperature of 40 °C, the steady state winding temperature was set to 80 °C. The load inertia was chosen to be about 15 % to 30 % of the rotor's inertia, which is reasonable for a pump or a conveyor belt application with a quadratic load characteristic[11].

When designing the synchronous reluctance machine the number of the reluctance rotor's air barriers was chosen to be four. Hereby the torque ripple at rated load was kept to about 30 %. To ease the manufacturing process, no rotor skewing was used, which in turn would decrease the torque ripple. A cut-off at the ends of each air barrier was introduced, as seen in Figure 3.2, to reduce the leakage inductance and losses in the rotor bars caused by the slot harmonics. Following two mechanical bridges for each air barrier were introduced to increase the rotor's mechanical strength. In Figures 3.1b and 3.2 the dark blue circles depict the chosen cage with a bar diameter of 4 mm. The ends of the bars are short circuited by a ring. These bars are placed in a manner that the flux paths are not significantly constraint and the leakage rotor flux is kept small. For example it can be seen that the bars are never totally surrounded by the rotor iron sheets. Moreover it can be seen that the cage is small compared to a complete filling of the air barriers. To reduce the losses in the cage caused by the slot harmonics even further, it is inserted towards the center

### 3. Line Start Machine Design

---

of the rotor. This insertion is inherent with a decrease of the synchronization capability. By these measures a high efficiency is achieved. For simplicity and an eased manufacturing process all cage bars are placed in the same radial distance from the rotor center. If more cage material would be used to reduce the rotor resistance, the synchronization performance increases, but the draw backs are increased rotor losses due to the slot harmonics and a bigger rotor inertia.

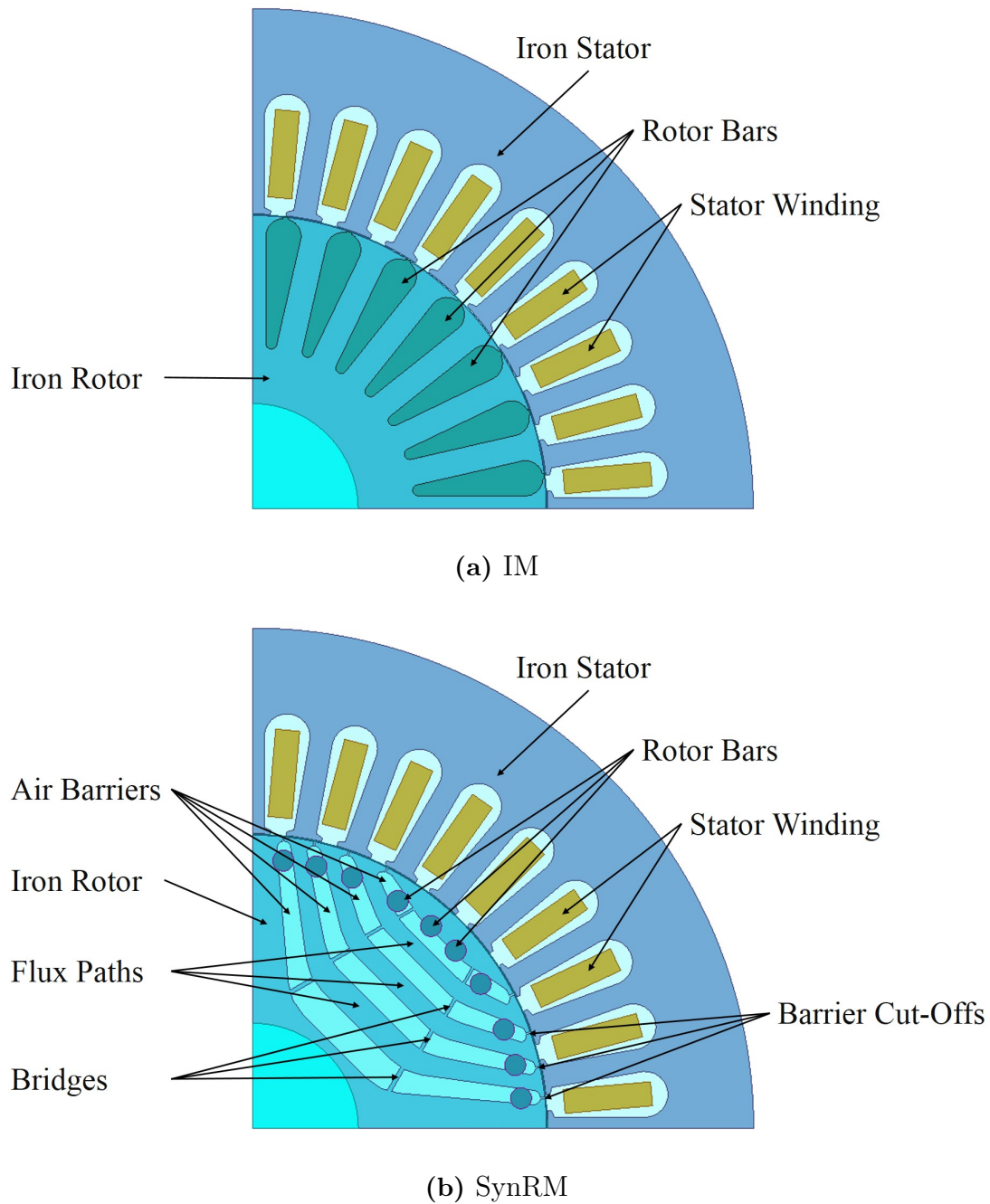


**Figure 3.1:** Induction (a) and synchronous reluctance(b) machine design for the four pole motor with 4kW rated output power.

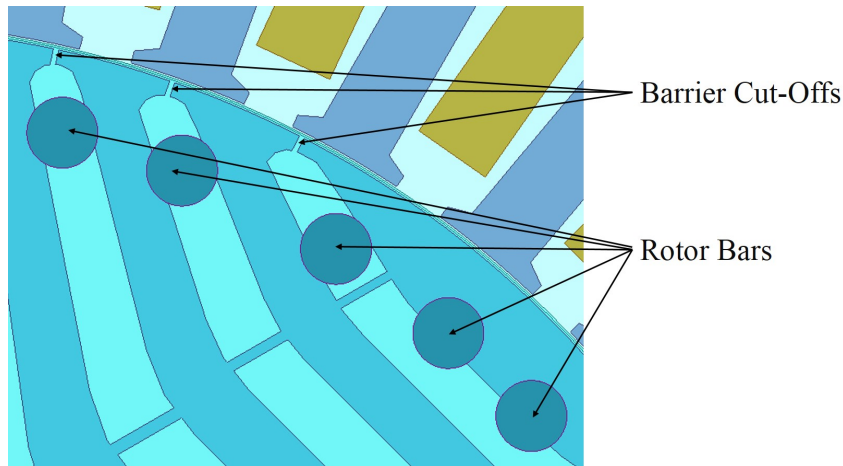


**Figure 3.2:** Rotor shape with barrier cut-offs.

A measure to achieve a lower rotor resistance for the depicted SynRM could be the usage of more cage bars, like for example in a double bar cage arrangement, which is not considered within the thesis work.

However to investigate the influence of the rotor resistance, the cage materials aluminium and copper were chosen. Hereby the copper achieves a lower cage resistance than aluminium. Through that the starting capability of the SynRM-Al is enhanced. The manufactured prototype line start reluctance machine rotors before soldering the end rings can be seen in Figure 3.3.

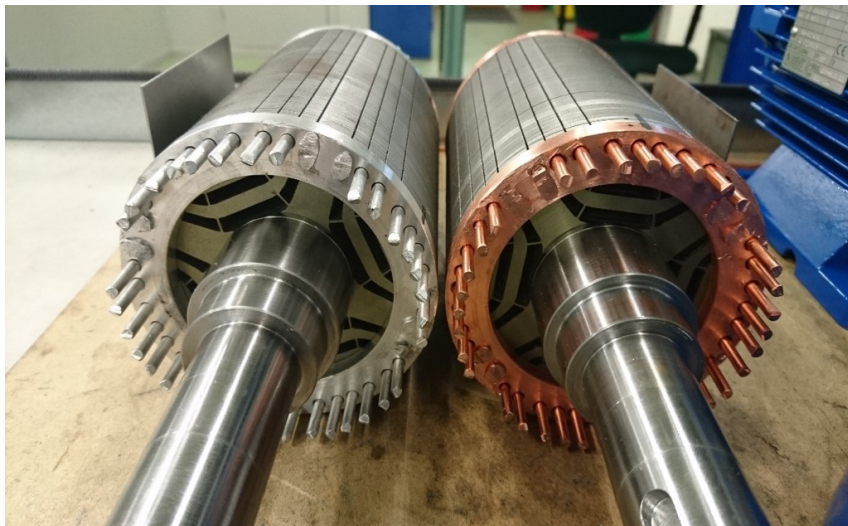


**Figure 3.3:** Line start SynRM rotors with aluminium(left) and copper(right) cage.

### 3. Line Start Machine Design

---

# 4

## Simulation Model and Test Setup

The following chapter gives a brief description about the used simulation model and the test bench setup used to conduct different load and starting tests on the test motors to determine the efficiency and the starting capability.

### 4.1 Simulation Model

For the simulations the FEM software ANSYS Maxwell is used. The excitation mode is set to voltage excitation 400 V three phase voltage, corresponding to the mains. The mechanical system is modeled as one stiff inertia and a constant torque load is used. The steel used and modeled is M470-50A. The cage is either modeled using aluminum or copper, whereby a temperature dependence of the conductivity is implemented. The final steady state winding temperatures and inertia values are taken from the actual test setup measurements.

#### 4.1.1 Solver Setting

For the determination of the efficiency values the simulation time step is set to 50  $\mu$ s, corresponding to a sample frequency of 20 kHz or 400 samples per electrical period. It was chosen in a manner that the harmonic content of the current and flux caused by the stator slots can be depicted with at least 20 samples per electrical period. From (4.1)[12] it can be seen that the order of the slot harmonics is dependent on the stator slots  $S$  and the number of machine poles  $P$ . For the test motors the order of the harmonic content is about 19, resulting in a frequency of 950 Hz.

$$n_{slot} = \frac{S \cdot 2}{P} \pm 1 = \frac{36 \cdot 2}{4} \pm 1 = 18 \pm 1 \quad (4.1)$$

When determining the starting capability the simulation time step is reduced to 0.5 ms, corresponding to a sample frequency of 2 kHz or 40 samples per electrical period. This measure was taken to reduce the computation time for each of the numerous simulation cases.

#### 4.1.2 Meshing

The used FEM mesh of the motor models can be seen in Figure 4.1. The applied mesh methods are length based, skin depth based and surface approximation. The air gap was meshed in three layers and the rotor bars were meshed finer and skin

depth layers were inserted. The generated meshes for the IM and line start SynRM comprise 6678 and 7354 elements, respectively.

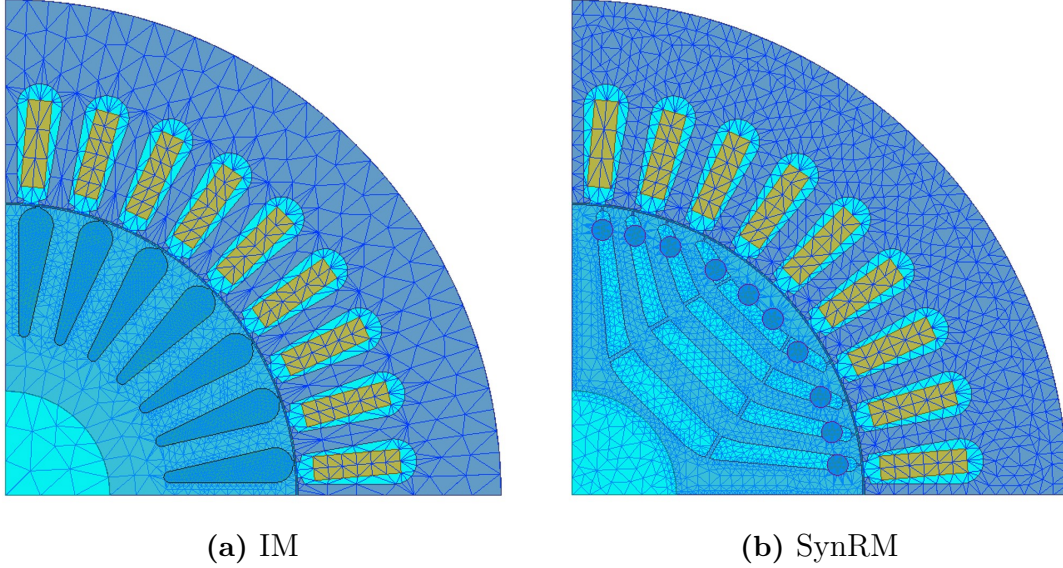


**Figure 4.1:** Mesh of the IM(a) and line start SynRM(b).

### 4.1.3 Efficiency and Power Factor Calculation

In general, the efficiency and power factor can be calculated by the ratio of input and output power and input and apparent power, respectively. At first the simulation models needed to be adapted regarding the influence of the laser cutting manufacturing process on the magnetic properties of the steel sheets as described in [13] [14]. Therefor the core losses were adapted, a load dependent stray loss and an increase of the phase current were introduced. The stray loss compensates also for the neglected end winding losses due to the usage of a simple 2D simulation model. According to [14] the core losses in the area of the stator teeth with a width of about 4.3 mm can be increased by about 50 %. Approximating that the core losses in the simulation are evenly distributed between stator and rotor, would lead to an actual core loss increase of 25 %. The stray loss factor was chosen to be 1 % at the rated load, whereby it is linearly dependent on the loading of the machine. Poor magnetic steel properties lead to a higher current and subsequently to a worse power factor. Hence the line currents in the simulation models are increased by the mean tolerance listed in [13] of about 3.5 %. The efficiency calculation can be seen in (4.2) and (4.3). Over a time span of  $n$  periods the average value of the efficiency is calculated under consideration of the introduced correction measures.

$$\eta = \frac{1}{n \cdot T} \int_{t_1}^{t_1+n \cdot T} \frac{p_{out}}{p_{in}} dt = \frac{1}{n \cdot T} \int_{t_1}^{t_1+n \cdot T} \frac{p_{mechanical}}{p_{electrical}} dt \quad (4.2)$$

$$\eta = \frac{1}{n \cdot T} \int_{t_1}^{t_1+n \cdot T} \frac{T_l \omega_r}{T_l \omega_r + p_{core} \cdot 1.25 + p_{solid} + p_{strand} + 40W \cdot \frac{T_l \omega_r}{P_{rat}}} dt \quad (4.3)$$

The calculation of the power factor can be seen in (4.4) to (4.6). Here the average active and reactive power are calculated over a time span of  $n$  periods.

$$\cos\phi = \frac{P}{S} = \frac{P}{\sqrt{P^2 + Q^2}} \quad (4.4)$$

$$P = \frac{1}{n \cdot T} \int_{t_1}^{t_1+n \cdot T} T_l \omega_r + p_{core} \cdot 1.25 + p_{solid} + p_{strand} + 40W \cdot \frac{T_l \omega_r}{P_{rat}} dt \quad (4.5)$$

$$Q = \frac{1}{n \cdot T} \int_{t_1}^{t_1+n \cdot T} \frac{1}{\sqrt{3}} [(v_b - v_c)i_a + (v_c - v_a)i_b + (v_a - v_b)i_c] dt \cdot 1.035 \quad (4.6)$$

## 4.2 Test Setup

The mechanical and electrical circuit of the test setup is depicted in Figure 4.2. As depicted, the test motor M1 is supplied via the contactor with the three phase main supply. The test motor's shaft is connected via a torque sensor P1 to the DC machine M2, which is used to apply a certain mechanical load to the test machine. The current  $I_d$ , which is proportional to the applied torque, is controlled by a three phase thyristor rectifier. The field current  $I_f$  is adjusted by an additional two phase thyristor rectifier. Both thyristor rectifiers are placed in one modular arrangement. To measure the temperature of the test machine's stator windings, each phase is equipped with a PT100 resistor.

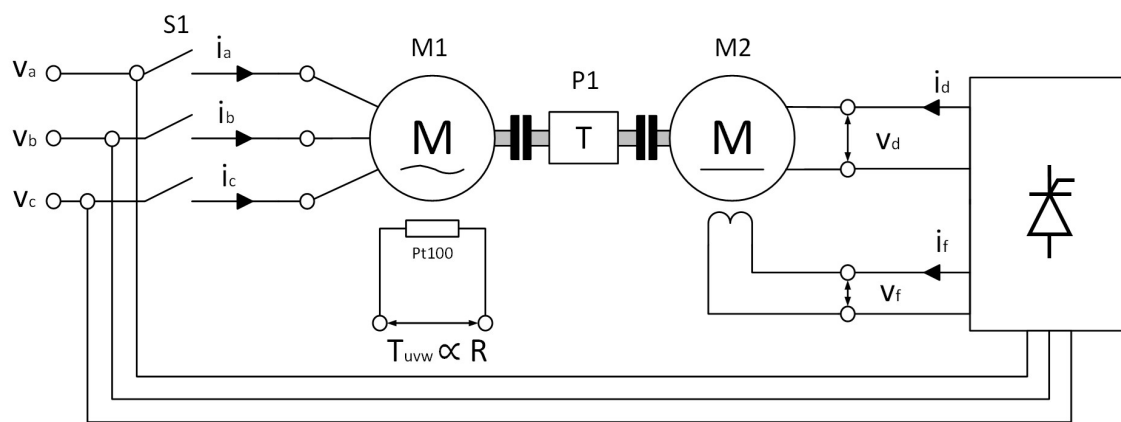


**Figure 4.2:** Schematic diagram of test setup including test motor M1 and DC machine M2.

The DC machine was chosen to have a similar power rating as the AC machines. Its rated power is 4.5 kW with a field current  $I_f$  of 1.89 A.

### 4.2.1 Testbench

The Figure 4.3 shows the test bench including test and load motor connected via the torque sensor. From the picture it can be seen that bulky clutches are used. The advantage of these is a high tolerance when aligning the setup, whereby these can be mounted easily. The drawback is the additional introduced inertia, which is undesired, because the synchronization capability is decreased.

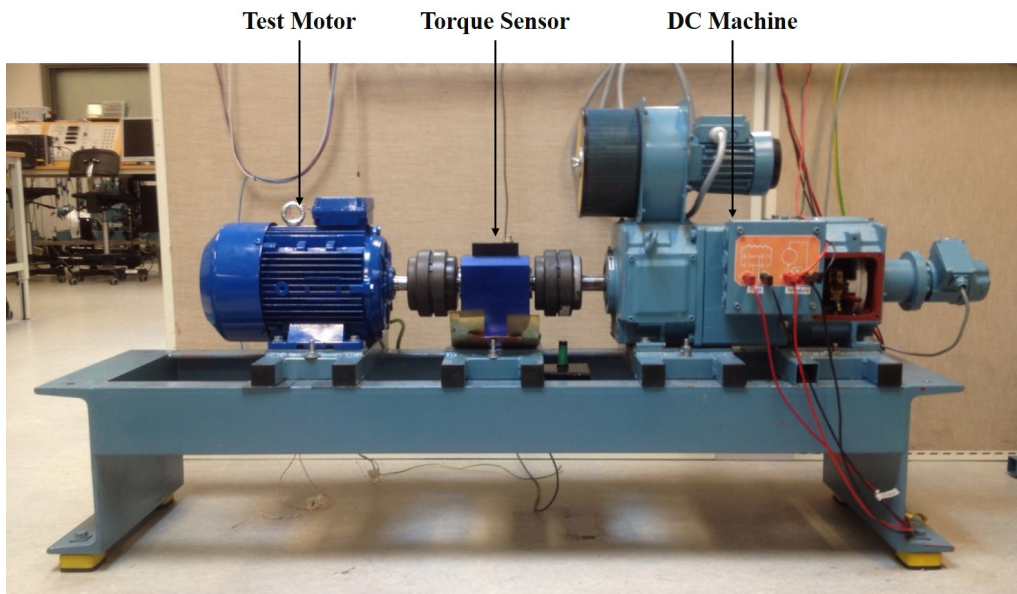


**Figure 4.3:** Motor test bench including test and load motor.

To investigate the dependence of the synchronization capability on the inertia, the torque sensor and the bulky clutches are replaced by a small clutch as depicted in Figure 4.4. Thereby the starting capability can be tested for two different system inertia values.

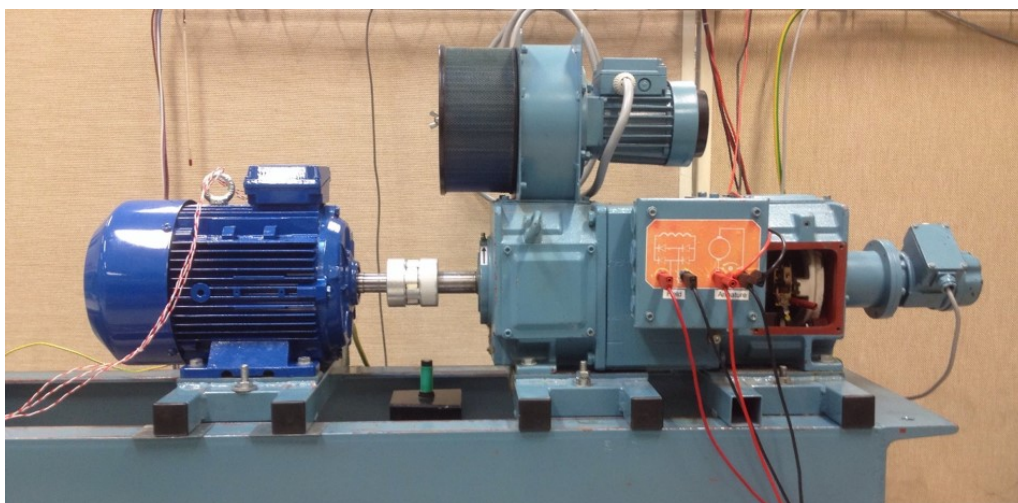


**Figure 4.4:** Motor test bench with reduced inertia.

### 4.2.2 Measurements and Control

To measure the temperature of the machine's stator windings a PT100 resistor is attached to each phase winding like in the example depicted in Figure 4.5. During the manufacturing process the resistors were placed in the end-winding region, which is commonly the hot spot of the windings. The sensors are fixed with a bandage and varnish. Finally its terminals are accessible over the wire connection, which is fed out.

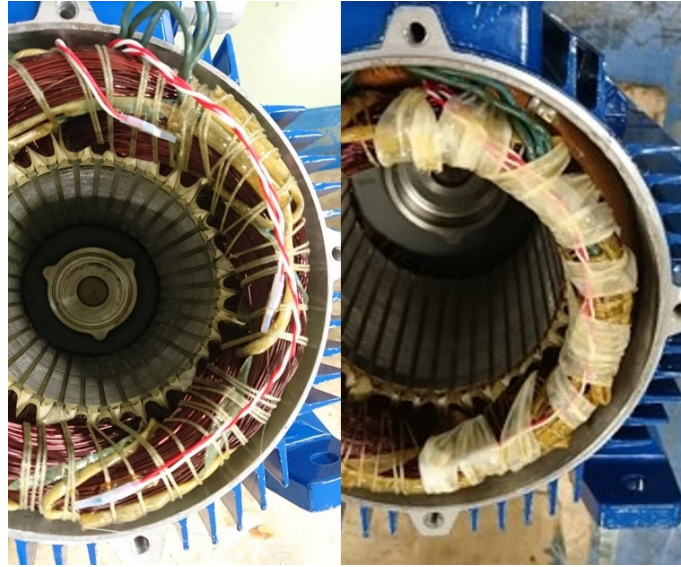


**Figure 4.5:** Placement and fixture of the temperature sensors in the end winding region.

Depending on the temperature the sensors' resistances will vary. To determine the actual temperature, the resistance values are transformed, using a transducer device, to voltage signals between 0 and +10 V, indicating 0 °C to +200 °C, respectively.

The phase and DC machine currents are measured using hall effect sensors. The current ratings of the used transducers is 35 A. Just for the current measurement in phase-c a 145 A rated sensor is used to investigate the starting current.

The used voltage probes have a rating of  $\pm 650$  V. Current and voltage values are transformed to proportional voltage signals within a range of  $\pm 10$  V, whereby those can be read directly by the used data acquisition system.

The range of the used torque meter is  $\pm 200$  N m with an output range of  $\pm 5$  V. For the chosen machines the torque meter can withstand even a direct start, despite the high dynamical starting torque. Additionally the torque meter is equipped with a pulse generator with 360 increments to obtain an accurate speed measurement compared to the attached tachometer. However the accuracy of the torque sensor's torque measurement is not sufficient to determine the efficiency properly. Therefore the mechanical steady state load torque is calculated by the DC machine currents and parameters.

Figure 4.6 shows the connection desk of the lab environment. The thyristor rectifier to steer and control the Dc machine, the contactor and the voltage and current

measurements devices are already embedded in the lab environment. The terminals of all devices can be easily accessed using banana connectors.

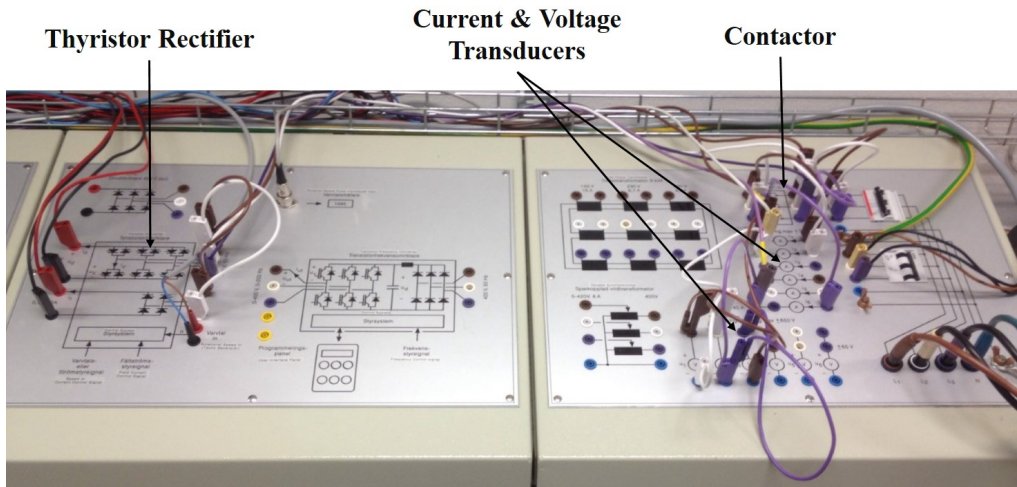


**Figure 4.6:** Test setup including both motors and torque sensor.

The test cabin, including the test bench and the electrical connection desk, can be seen in Figure 4.7. The transducers for the PT100 elements are placed on a separate table adjacent to the motor bench. The measurement signals are feed forwarded to the acquisition system using BNC cables .

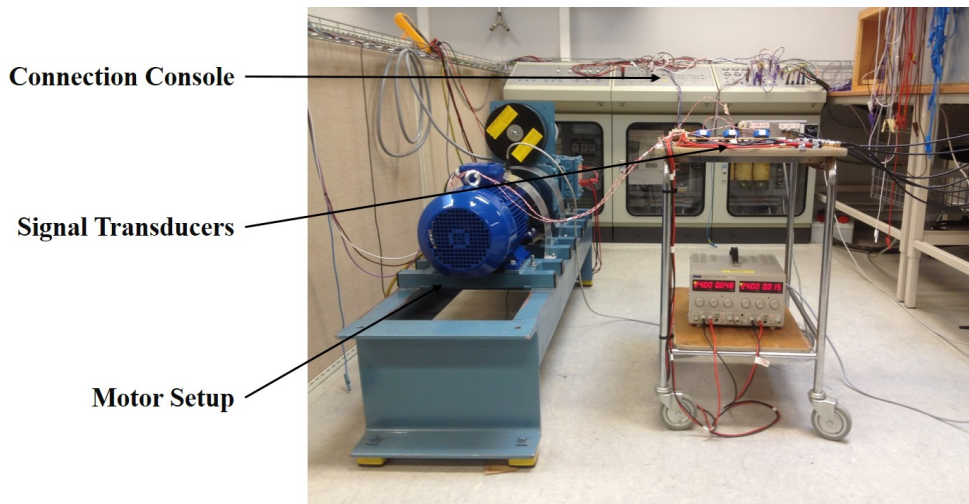


**Figure 4.7:** Connection desk of the electrical setup.

Figure 4.8 shows the control desk of the setup. The right hand part contains the voltage and current measurements, which are feed over BNC cables to the data acquisition system. The part in the center is used to control the DC machine and the contactor to start the test motors. The DC machine can be controlled either in speed or current control. The operation of the bench can be executed manually or externally, steered by the computer.

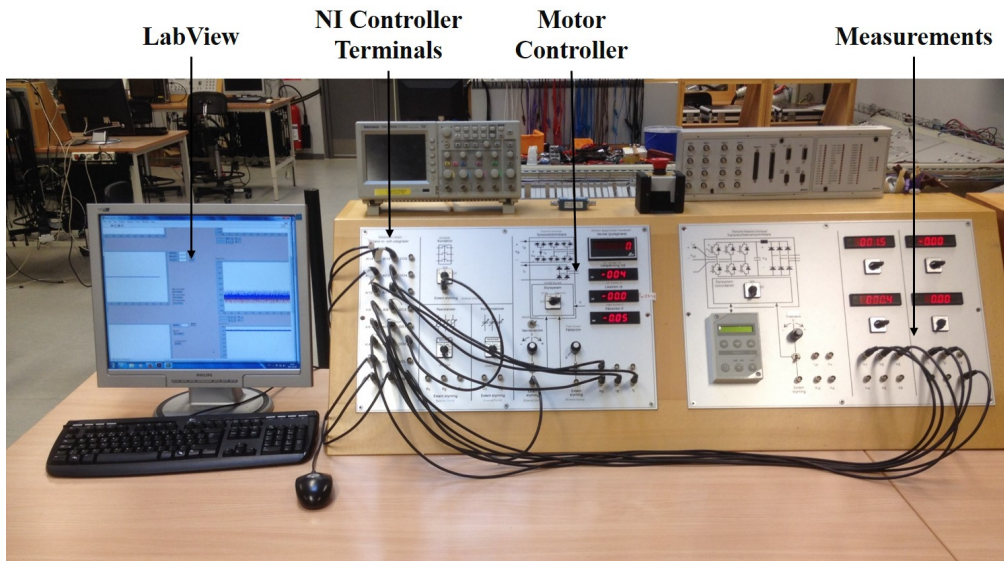


**Figure 4.8:** Control desk of the test setup.

### 4.2.3 Implementation in LabView

To acquire the measured data and to control the DC machine and the contactor, the I/O controller MIO16E4(6040E) of National Instruments is used. The controller is integrated on a PCI card, which is mounted in the computer used in the lab-setup. The controller comprises 16 analogue inputs with an input range varying from  $\pm 0.5$  V to  $\pm 10$  V, which are used to measure the current, voltage, speed and torque waveforms. The resolution of each input channel is 12 bit and one common ground is shared. To control the DC machine one of the two analogue 12 bit  $\pm 10$  V outputs is used. Additionally the controller comprises 8 digital outputs, whereby one is used for the contactor maneuver. The sampling frequency of 30 kHz is chosen to capture also the slot harmonic content[12] of the current waveforms and ensuring a stable operation of the controller. Only when determining the machines' thermal time constant the sampling frequency is set to 0.5 Hz to reduce the amount of captured data.

The used controller is programmed using National Instrument's software LabView. The Figure 4.9 depicts a schematic diagram of the implemented program. Before starting the actual test and measurement algorithm, the offset values of each input channel needs to be determined. Therefore a certain amount of samples is captured before running up the machines and subsequently the average value is subtracted constantly during normal operation. The followed test process can either consist of a single sequence or an iterative procedure. During the iterative procedure a certain amount of samples is captured and can be monitored online for each iteration. The contactor maneuver and the control of the DC machine are done manually during operation. Via a manual control button in the software the sampled data during one iteration can be written to a data sheet. When determining the efficiency values this procedure is used. During the single sequence procedure, the current profile of the field current  $I_f$  and the instant of contactor maneuver is programmed. The measurements are taken in parallel and finally written to a data sheet. This

procedure is used to observe the starting process or determine the starting capability.

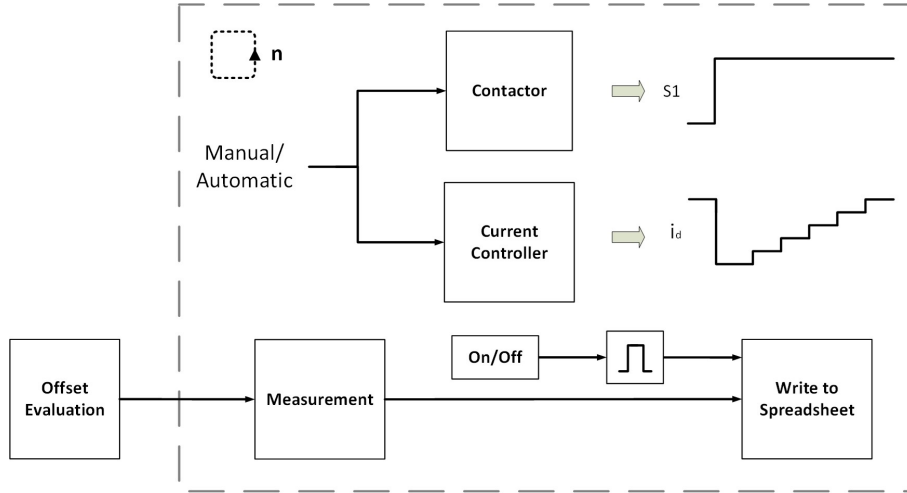


**Figure 4.9:** Schematic diagram of implemented LabView program.

#### 4.2.4 Efficiency and Power Factor Calculation

The efficiency values of the test motors, using the test bench, were determined by the mechanical output and electrical input power, whereby the output was calculated by the DC machine currents and parameters. The governing equations of the electrical and mechanical characteristics of the DC machine are depicted in (4.7) and (4.8), respectively.

$$V_d = R_d i_d + L \frac{di_d}{dt} + \omega_r k_\phi \quad (4.7)$$

$$J \frac{d\omega}{dt} = T_e - T_{l-extra} - B\omega_r \quad (4.8)$$

Following, the efficiency was determined as an average value of the in- and output power over a time span of  $n$  periods as seen in (4.9). The output power was determined by the flux constant, DC machine current  $I_d$  and the damping constant  $B$ , whereas the input power was calculated by the line voltages and currents.

$$\eta = \frac{1}{n \cdot T} \int_{t_1}^{t_1+n \cdot T} \frac{(k_\phi I_d + B\omega_r)\omega_r}{v_a i_a + v_b i_b + v_c i_c} dt \quad (4.9)$$

The power factor as the ratio of active and apparent power, was determined as depicted in equation (4.10) to (4.10). Also here the average value over an interval of  $n$  periods is considered. Input and output power are determined by the line current and phase voltage quantities.

$$\cos\phi = \frac{P}{S} = \frac{P}{\sqrt{P^2 + Q^2}} \quad (4.10)$$

$$P = \frac{1}{n \cdot T} \int_{t_1}^{t_1+n \cdot T} [v_a i_a + v_b i_b + v_c i_c] dt \quad (4.11)$$

$$Q = \frac{1}{n \cdot T} \int_{t_1}^{t_1+n \cdot T} \frac{1}{\sqrt{3}} [(v_b - v_c)i_a + (v_c - v_a)i_b + (v_a - v_b)i_c] dt \quad (4.12)$$

# 5

## Measurement and Simulation Results

The following chapter presents the gained results from the measurements and simulations. Further it is described how the information from the measurements are implemented in the simulation model.

### 5.1 Test Bench and Setup Parameters

The flux constant  $k_\phi$  and the damping constant  $B$ , seen in (4.7) and (4.8), are important measures to determine the load represented by the DC machine, when running the actual test motors. To determine the flux constant the armature resistance  $R_d$  needed to be determined first. Therefor a DC voltage was applied to the machines terminals, whereby the armature inductance could be neglected at steady state and the resistance was calculated by the measured current and voltage as seen in. (5.1). Subsequently the flux constant was determined by running the DC machine in no load operation at 1440 rpm, while the field current  $I_f$  was set to 1.89 A. Finally the flux constant was determined by the measured current and voltage as in (5.2).

$$R_d = \frac{V_d}{I_d} = \frac{9.94 \text{ V}}{5.25 \text{ A}} = 1.893 \Omega \quad (5.1)$$

$$k_\phi = \frac{V_d - R_d I_a}{\omega_r} = \frac{218.1 \text{ V} - 1.893 \Omega \cdot 1.113 \text{ A}}{1440 \frac{2\pi}{60} \text{ rad s}^{-1}} = 1.4323 \text{ N m A}^{-1} \quad (5.2)$$

Furthermore the damping constant of the system for each motor setup needed to be determined. For this purpose the DC machine was operated in no load. Hereby the machine was run for at least one hour, since the viscosity of the lubricant in the bearings is temperature dependent. The damping constant was then calculated as in (5.3) and the final values are depicted in Table 5.1.

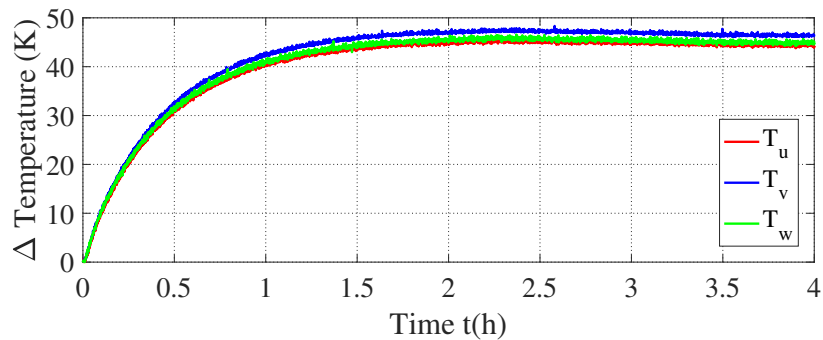
$$B = \frac{T_e}{\omega_r} = \frac{k_\phi I_d}{\omega_r} \quad (5.3)$$

**Table 5.1:** Viscous damping constant  $B$

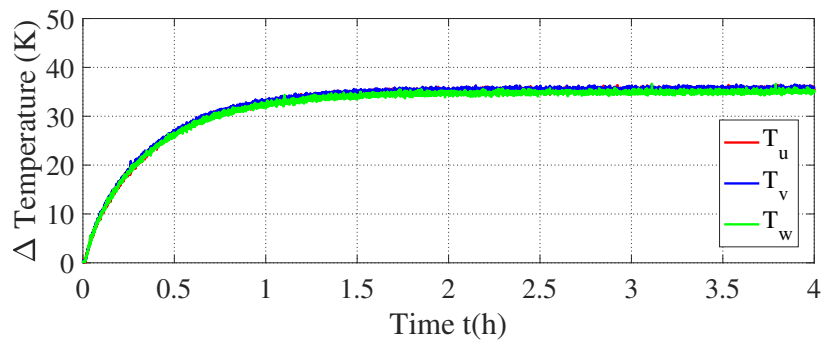
Machine Setup	Damping B (Nm/ rad s <sup>-1</sup> )
SynRM-Al	0.0081
SynRM-Cu	0.0084
IM	0.0078

## 5.2 Steady State Temperature

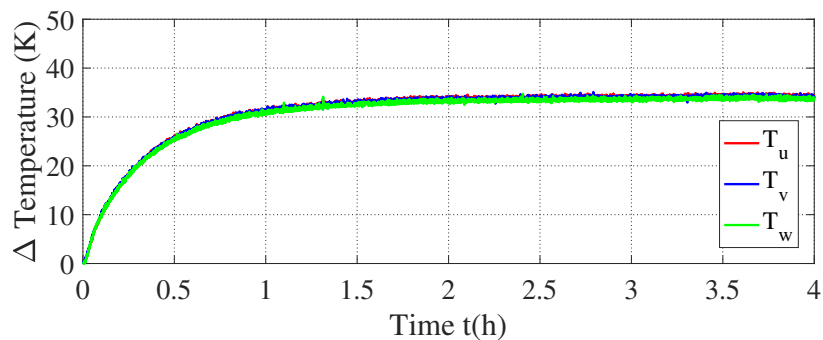
To measure the efficiency of the motors the thermal steady state must be reached, since the stator winding and rotor bar resistances are temperature dependent, which in turn affect the obtained efficiency. Therefore the thermal behaviour of the test machines needs to be measured firstly to obtain the thermal time constant of the system. Figure 5.1 shows the measured stator winding temperatures of the test motors when running with rated mechanical load of 4 kW over a time span of four hours.



(a) IM



(b) SynRM-Cu



(c) SynRM-Al

**Figure 5.1:** Stator winding temperature rise for the three test machines when running on rated load.

It can be seen that the temperature follows the shape of a first order system. The

steady state temperature is reached after around two and a half to three hours. For this reason all measurements regarding the efficiency were taken after running the machines, for different loadings, for three hours. From Figure 5.1 it can be seen that the terminal temperatures for the synchronous reluctance machines are less than for the IM. This indicates already reduced losses. The final temperature rise for the IM and the SynRMs are about 37 K and 47 K, respectively.

When measuring the efficiency values for all machines at different loadings the terminal winding temperatures were obtained as well. The Figure 5.2 shows the terminal mean stator winding temperatures for all three machines, depicted with blue dots, while the laboratory temperature was about 21 °C. Subsequently the temperature in dependence of the loading was approximated by a quadratic equation with the form seen in equation (5.4).

$$T(L) = A \cdot L^2 + B \quad (5.4)$$

The dashed plots in Figure 5.2 depict the approximated temperature behaviour for each machine, which in turn was implemented in the simulation model.

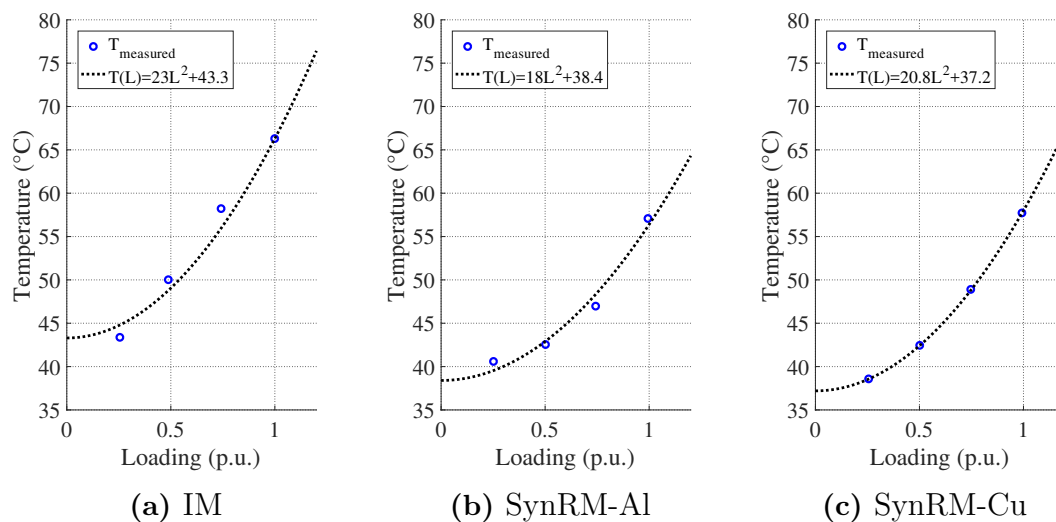


**Figure 5.2:** Mean stator winding temperature for different loadings measured and approximated.

### 5.3 Efficiency and Power Factor

Like mentioned in the previous section, the steady state stator winding temperatures gained from the efficiency measurements conducted on the test bench were used to approximate the temperature-loading functions, which in turn were implemented in the simulation model to finally obtain the simulated efficiency and power factor values. Figures 5.3a, 5.3b and 5.3c show the determined simulation and measurement results for the efficiency of the three motors. It can be seen that the efficiency values of the synchronous reluctance machines are roughly about 2 %-3 % higher than of the IM. It can be seen that the simulation and measurement result agree for the loading range from 25 % to 100 %. The SynRMs show a slightly higher deviation regarding the simulation and the measurement around 25 % loading. Nevertheless it can be seen that the obtained results, simulated and measured, show a similar behaviour.

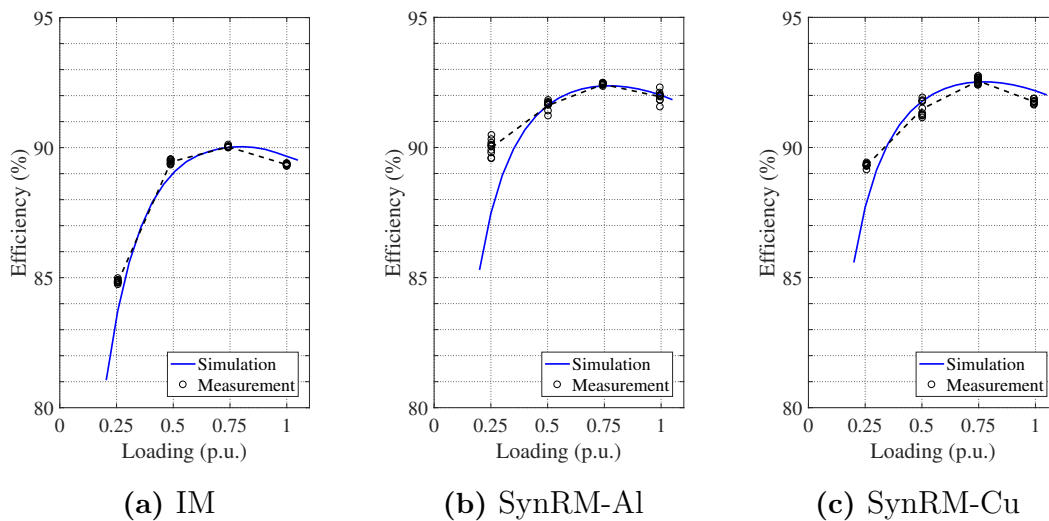


**Figure 5.3:** Efficiency simulation and measurement results for all three machines for different loadings.

The results for different loadings are depicted in Table 5.2 as well. It can be seen that the efficiency improvement at rated load is around 2.5 % to 2.7 %. Following it can be stated that both SR motors fulfill the needed efficiency criteria of 91.1 %, for a 4 kW four pole line start machine, to achieve an IE4 efficiency rating.

**Table 5.2:** Motor efficiency for different loading.

Loading	$\eta$ (%)					
	IM		SynRM-Al		SynRM-Cu	
	Sim	Meas	Sim	Meas	Sim	Meas
0.25	83.7	84.9	87.5	90.0	87.7	89.3
0.50	89.1	89.5	91.6	91.6	91.8	91.5
0.75	90.0	90.1	92.4	92.4	92.5	92.6
1.00	89.7	89.3	92.0	92.0	92.2	91.8

The power factor values for the three machines are depicted in Figure 5.4. It can be seen that the power factor increases with the loading and shows a kind of a knee point around rated load. The measured and simulated power factor for the SR machines shows a deviation like a constant offset. Considering the complex rotor structure of the SR machine, the influence of the laser cutting on the magnetic behaviour seems to be higher than for the IM leading to a higher reactive current drawn from the mains. On the other hand the reduced power factor in the SR machines compared to the IM is due to the reason that the active power drawn from the grid is reduced, whereas the reactive is increased, since less iron material is used in the SR machines' rotors.

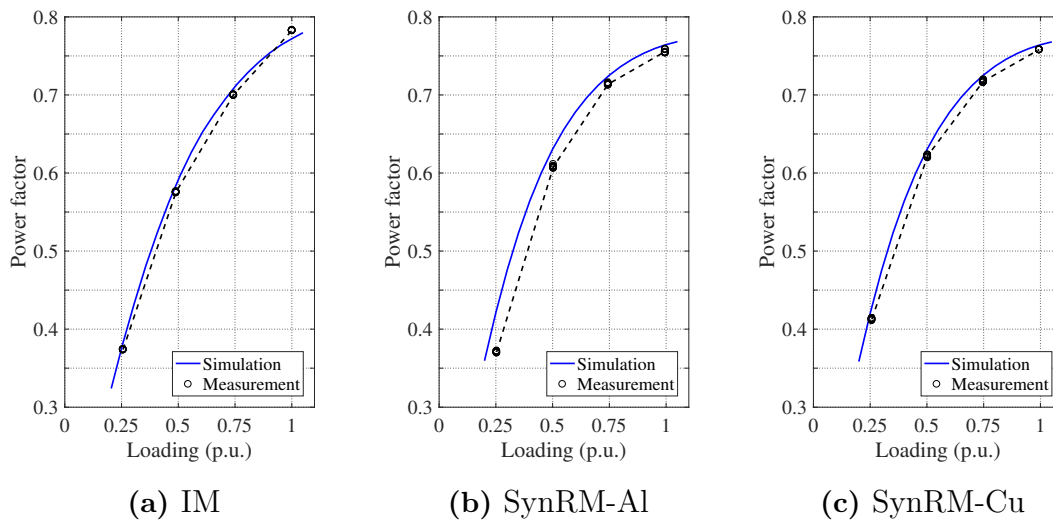


**Figure 5.4:** Power factor simulation and measurement results for all three machines for different loadings.

The power factor of the three machines for different loadings is additionally depicted in Table 5.3.

**Table 5.3:** Motor power factor for different loading.

Loading	$\cos(\phi)$					
	IM		SynRM-Al		SynRM-Cu	
	Sim	Meas	Sim	Meas	Sim	Meas
0.25	0.38	0.37	0.42	0.37	0.42	0.41
0.50	0.60	0.58	0.63	0.61	0.63	0.62
0.75	0.71	0.71	0.73	0.71	0.73	0.72
1.00	0.77	0.78	0.76	0.76	0.76	0.76

## 5.4 Inertia

The synchronization capability of the SR machines can be described as a function of the maximal load torque with respect to the inertia, whereat the machine should still be able to reach synchronism. To determine the synchronization capability experimentally, the inertia needs to be determined at first. For this purpose a high current step can be applied without loading the machine, whereby the effect of the damping  $B$  can be neglected. Following the mechanical system equation, depicted in (4.8), can be simplified to (5.5) to estimate the rotating shaft's inertia.

$$J = \frac{T_e}{\frac{\omega_r(t_2) - \omega_r(t_1)}{t_2 - t_1}} \quad (5.5)$$

Figure 5.5 shows an example of the current and speed measurements for a current step of 20 A. It can be seen that the current follows the shape of a first order system and it reaches its reference at about 0.2 s. Further a delay is visible between the reference and the beginning of the rise in the current. When the current reference is reached the acceleration seems to be constant.

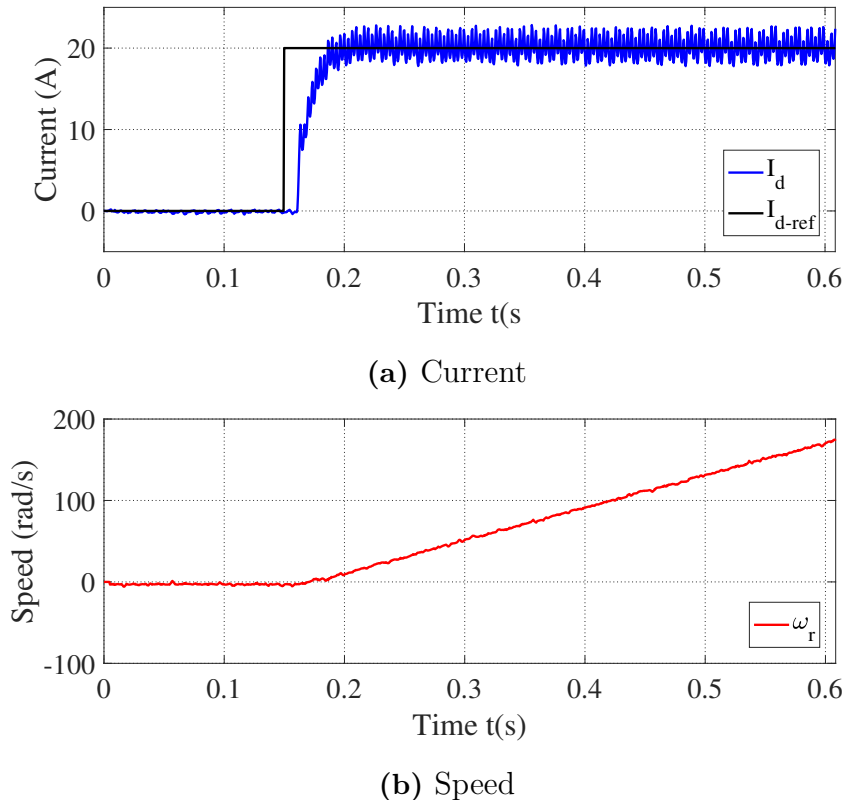


**Figure 5.5:** Current(a) and Speed(b) for the different setups with respect to the displacement angle  $\delta$ .

To determine the starting capability, at least for two different inertia values, the torque sensor was dismantled and the DC machine was directly connected to the

test motors. The results obtained for the system's inertia for the different machine setups with and without the torque sensor can be seen in Table 5.4 and Table 5.5.

**Table 5.4:** System inertia with torque sensor.

Machine Type	Inertia J (kg m <sup>2</sup> )
IM	0.070718
SynRM-Al	0.068225
SynRM-Cu	0.070616

**Table 5.5:** System inertia without torque sensor.

Machine Type	Inertia J (kg m <sup>2</sup> )
IM	0.045654
SynRM-Al	0.042946
SynRM-Cu	0.045843

The rotors' inertia values for all machines can be seen in Table 5.6. Therefore the DC machine's rotor inertia needed to be determined first, which is subsequently subtracted from the values seen in Table 5.5.

**Table 5.6:** Inertia of the machines' rotors.

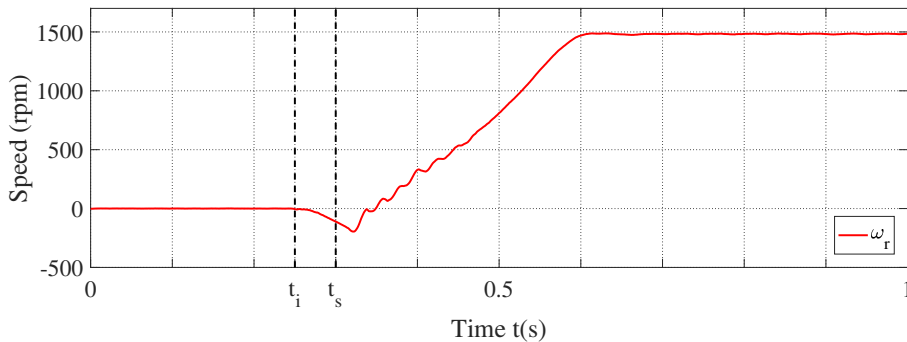
Machine Type	Inertia J (kg m <sup>2</sup> )
DC machine	0.029606
IM	0.016048
SynRM-Al	0.013340
SynRM-Cu	0.016237

## 5.5 Synchronization Capability

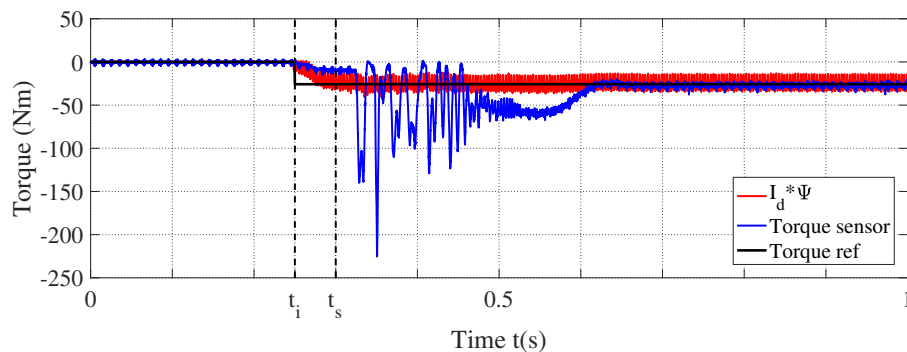
Within this section the starting performance results of the IM and the synchronization capability results of the SR machines are presented.

### 5.5.1 Start Capability - IM

In terms of an induction machine it cannot be referred to its synchronization capability, because it always runs with slip. Therefore the term starting capability is used instead. The following graphs in Figure 5.6 illustrate the measured start process of the IM, when loaded with a constant torque load corresponding to the rated load. This depicted example should just emphasize the strong starting performance of the IM. The inertia of the system is about  $0.07 \text{ kg m}^2$ , as seen in Table 5.4. At the instant  $t_i$  the current controller reference is stepped to rated load, about 17.5 A. After a time delay of 50 ms at the instant  $t_s$  the contactor maneuver is triggered to start the IM. Through the time delay the current  $I_d$  can reach the reference before the contactor is closing, whereby the machine starts with a constant load. It can be seen that the IM has no problems to start even if the machine is loaded with rated load during run up. Final speed is reached at around 1460 rpm. Final speed is reached at around 1460 rpm.



(a) Speed



(b) Torque

**Figure 5.6:** Speed(a) and torque(b) during the start up of the IM, if rated load is applied.

Additionally Figure 5.6b depicts the transient torque measured by the torque meter.

Due to this typically high torque transient it was not possible to use a torque sensor with a lower torque limit, which in turn would have had a higher measurement accuracy and could have been used for the efficiency determination. Nonetheless it is seen that the IM has no difficulties to start with a high inertia and rated load torque, which indicates the strong starting capability of the IM.

### 5.5.2 Synchronization Capability - LS-SynRM

An indication of the synchronization capability of the SR machines can be seen in the reluctance torque curve and the slip torque of the line start synchronous reluctance machines. A high reluctance pull-out torque and a low slip speed characterize a good synchronization capability.

Figure 5.7 depicts the reluctance torque in dependence of the load angle, when synchronization is reached, and the cage torque contribution for different slip speeds for both SR machines. All plots were obtained from the simulation model. The reluctance torque for both machines is independent of the cage material. At steady state it can be approximated in form as described in (2.22). It can be seen that the pull-out torque is about twice the rated load torque (25.4 N m). On the contrary the cage torque of the machines deviates, depending on the cage material. Both torque curves have a similar shape with a pull-out torque occurring around half speed, whereas a second local maximum is located between 1000 rpm and 1250 rpm. In the region close to zero slip the copper machine shows a higher torque, which indicates an already better synchronization capability for the copper cage machine. However the initial torque of the SynRM-Cu is lower, indicating that the copper machine cannot even start with the rated load torque.

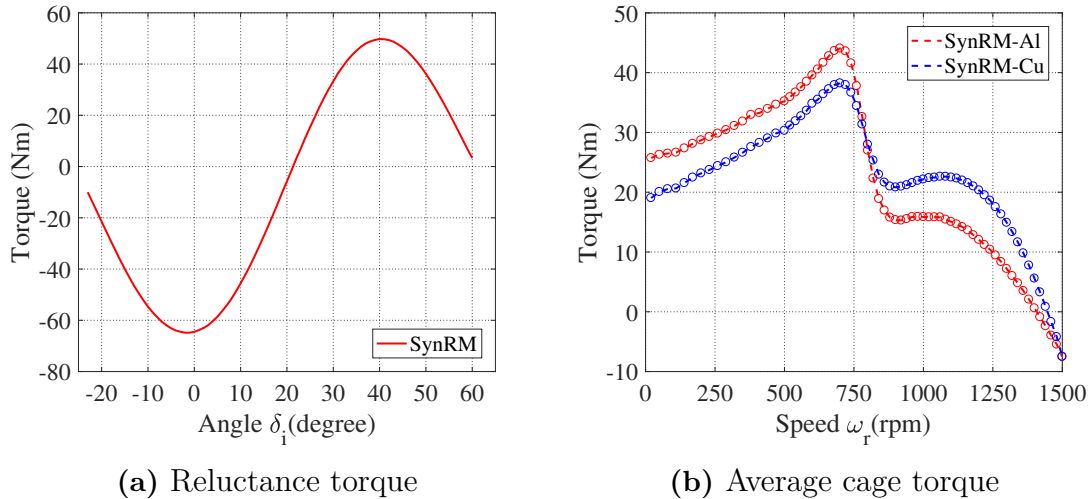
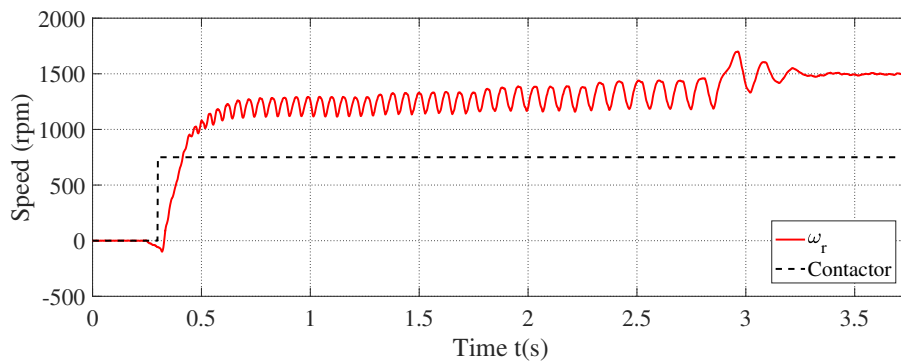


**Figure 5.7:** Reluctance torque at steady state(a) and cage torque at different slip speeds(b) .

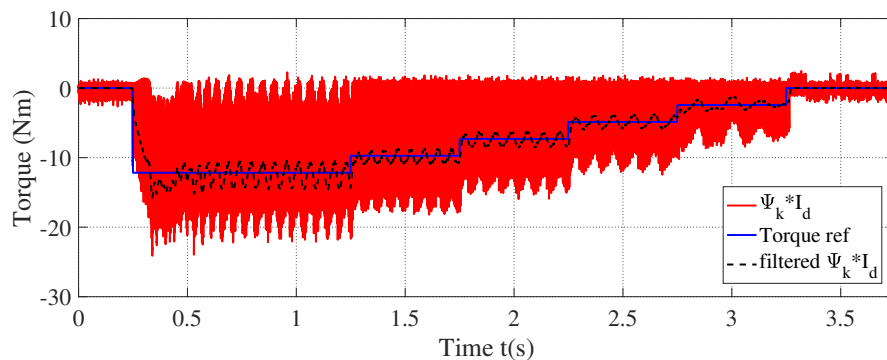
To measure the SR machines' starting capability, a torque load in form of a constant current  $I_d$  is applied. The load is firstly stepped and subsequently successively reduced by steps corresponding to 10% of the rated load. Meanwhile current and speed waveforms are monitored to determine the load level that the machine is able

## 5. Measurement and Simulation Results

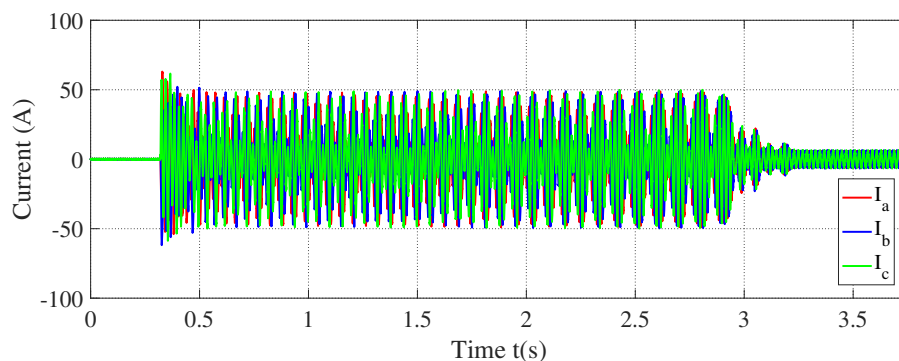
to synchronize. Running the machines for too long with slip can lead to a severe rotor damage. For this reason the time intervals are chosen to keep the time at slip speed as short as possible. The first load interval is designated to have a duration of 1 s, since the speed has to reach the slip speed from standstill. All other time intervals are chosen to be 0.5 s. The Figure 5.8 shows the synchronization test for the SynRM-Al machine with an inertia of about  $0.7 \text{ kg m}^2$ . The DC machine's current was initially stepped to about 50 % of the rated load. The speed during the test can be seen in Figure 5.9c and the load torque is depicted in Figure 5.8b, while the SR machine's current is seen in Figure 5.8c.



(a) Speed



(b) Torque

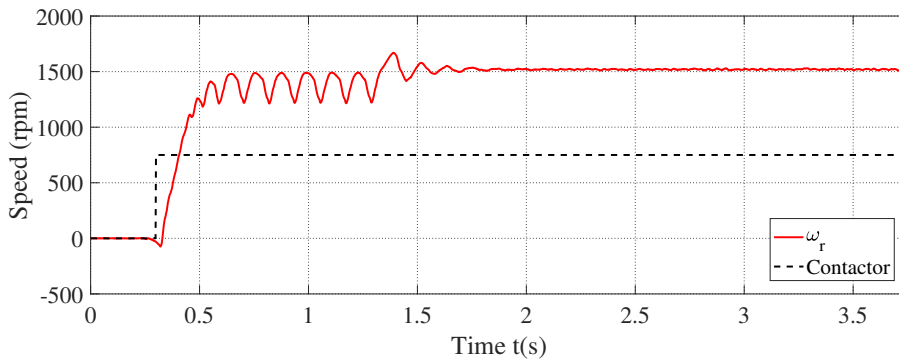


(c) Current

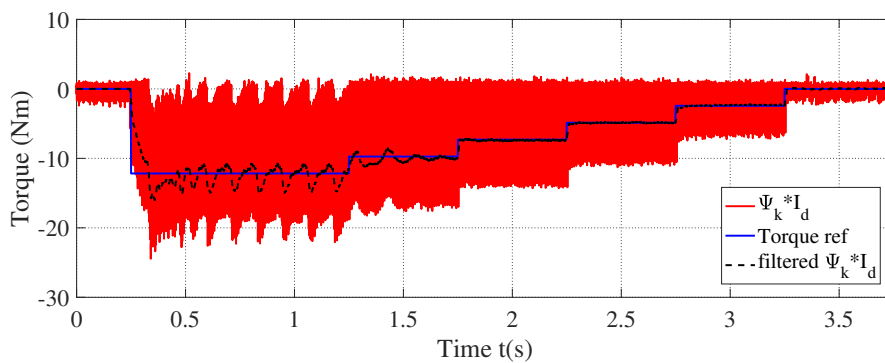
**Figure 5.8:** Synchronization capability measurement for the SynRM-Al.

After the contactor closes, the speed increases and the machine is running on slip

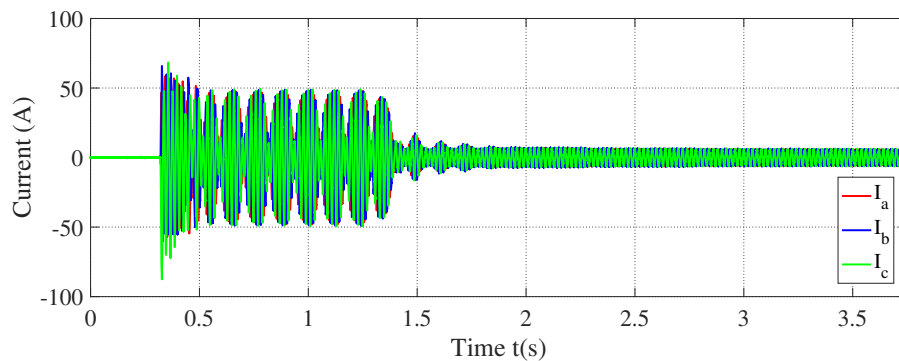
speed until the load current  $I_d$  reaches 10% and the machine exceeds synchronous speed at around 2.8s. The DC machine's load torque calculated by current and flux constant of the DC machine oscillates. The AC machine is such a big disturbance that the current controller can not keep the oscillations small. However the moving average corresponds to the reference. Additionally it is seen that the three phase currents drawn from the mains during slip speed are high, which in turn results in a high power dissipation in the rotor bars. This power dissipation corresponds to a multiple of the rated motor power, whereby the rotor cage is mechanically stressed through the thermal expansion of the rotor bars, which in turn can lead to a disruption of the cage. Thus the machine should not run with slip for too long.



(a) Speed



(b) Torque



(c) Current

**Figure 5.9:** Synchronization capability measurement for the SynRM-Cu.

Subsequently the same procedure is repeated for the SynRM-Cu and can be seen in Figure 5.9. Compared to the SynRM-Al synchronization is reached at about 40% load level. Additionally the synchronization capability was measured for both machines with a reduced inertia excluding the torque sensor.

The final results of the synchronization capability can be seen in Figure 5.10. The depicted load torque takes here the damping  $B$  into account. In the graphs the simulated boundary is depicted in blue. The system is just able to reach synchronism, if a combination of inertia and start torque below the blue curve is applied. The measured values are marked with a black "x" for an unsuccessful and with a black "o" for a successful synchronization. It can be seen that the measurements comply with the simulations.

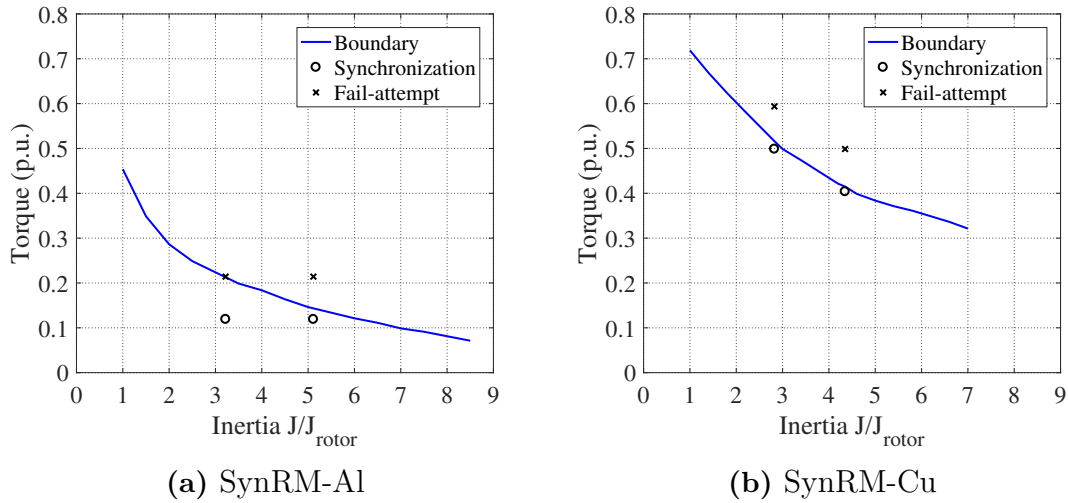


**Figure 5.10:** Synchronization capability of the SR machines.

Nevertheless it is seen that both machines are not able to synchronize, if started under rated load conditions. The maximum load torque, ensuring a successful synchronization for the SynRM-Al and the SynRM-Cu occurs, if the load inertia is technically zero corresponding to about 45% and 70% of the rated load torque, respectively. Subsequently the synchronization capability is decreasing with respect to the load inertia. The depicted behavior shows that the synchronization capability of the SR machines is poor. Considering the starting behaviour, the SR machines cannot compete with the IM.

Regarding the pull-out torque of the SR machines, it was not possible to measure this, since the rated torque of the DC machine was just about 30 N m, which is far less than the simulated pull-out torque seen in Figure 5.7a.

# 6

## Conclusion

Within the frame of this thesis the line start synchronous reluctance machines and the benchmark induction machine were tested regarding the efficiency, power factor and starting capability. For the tests a simulation model, built in the FEM software ANSYS Maxwell, was used and a test bench setup for the first prototypes and the benchmark product were concluded.

It can be said that the simulation results complied with the obtained measurements. The simulation models give a good prediction of the actual motor behaviour regarding efficiency, power factor and starting capability. It can be used for further test cases and design adaptations regarding the rotor geometry.

Regarding the reluctance machines a reduction of the motor losses about up to 27.6% at rated load, compared to the induction machine, was achieved. On the opposite the power factor of the SR machines was slightly less than compared to the IM. Regarding the power factor the simulation model had a small discrepancy referring to the SR machines. The influence of the cutting effect on the magnetic properties of the steel sheets was taken into account for all three machines in a similar manner. However the rotor structure of the SR machines is more complex and contains more cut edges, which in turn explains the deviation of the simulation results compared to the measurements.

The starting capability of the induction machine is independent of the load inertia, considering reasonable inertia values. The inertia just influences the time reaching final slip speed, but the final slip speed is solely dependent on the load torque. The strong starting capability is one of the major advantages of the IM compared to the prototype SR machines. When starting the SR machines, synchronism must be reached to avoid high losses in the rotor bars, which in turn can destroy the machine. However it was seen that the synchronisation capability of the SR machines is just acceptable for low load inertia values and a small load torque. The copper cage, comprising a lower rotor resistance, had a better synchronization capability than the aluminum cage machine. Nevertheless the range of possible applications of the SR machines is quite limited compared to the IM.

Some reasonable applications could be low inertia drives or applications, where the SR machines can be started under no load condition, like for example in an unloaded conveyor belt, a fan with a pitchable impeller or a pump with a throttle valve.



# 7

## Discussion and Future Work

From the the results it was seen that the efficiency enhancement of the SR machines resulted theoretically in a higher efficiency rating. However the starting capability was poor. The SR machines are not able to synchronize with a high load inertia or if fully loaded during start up.

However as part of a future work the start performance for a quadratic load should be determined, which is typical for the majority of industrial applications. Furthermore the SR machines should be tested in actual application environments.

Within the frame of the thesis the improvement of the stator design was not considered. The relatively high stator resistance has a significant influence on the synchronization capability. Regarding the design, a shortening of the SR machines' length and an increase in the frame size could result in a better synchronization capability. If the number of stator winding turns is kept, the stator resistance and the rotor resistance would be decreased. Thereby the cage torque would contribute to a slip speed closer to synchronism. Hereby also the magnetizing inductance would be decreased, but it was seen that there was still a margin of the reluctance pull-out torque with respect to the nominal load torque.

Further the cage design should be optimized to achieve symmetrical rotor resistances in dq-quantities. Additionally a rotor skewing should be applied and ferrite magnets could be inserted to achieve a better power factor, and following a better efficiency.

### 7.1 Sustainability and Ethical Aspects

Within the frame of the thesis it was shown how the efficiency of a common induction machine can be easily improved by a rotor adaption. This line start reluctance principle could be applied to various kinds of induction machines, whereby the efficiency enhancement would lead to less consumed electrical energy and following less  $CO_2$  emissions, assuming the energy is produced by oil, coal or natural gas. Another advantage of the machine is its robustness, since it does not need any brushes. The assistance by permanent magnets could lead to a better power factor and a better efficiency rating. Hereby just ferrite magnets should be used, because the assessment of a sustainable product should also consider the materials used in it, how those are mined and further processed, the conditions for the labors and the overall influence on the environment. Within the design of the SR machines the use of rare earth materials was deliberately avoided due to several ethical reasons, which are discussed in the subsequent section.

### 7.1.1 Rare Earth Materials

Nowadays rare earth materials are frequently used in electrical machines and electronic devices. Especially in the field of electric machines a multiple times higher power density, compared to the usage of ferrite magnets, can be achieved. In this context Neodym and Samarium Cobalt belong to the most common types used for electrical machinery in supposedly green technologies as in hybrid vehicles or wind power plant generators.

Nevertheless the mining for these materials take a lot of effort and causes often a tremendous ecological damage, if the necessary environmental precautions are not taken properly. Commonly rare earth materials can be found as a by-product when mining for iron. The iron oar contains small amounts of different rare earth materials, which needs to be separated. This preparation takes a lot of effort, whereby toxic chemicals and acids are used. Furthermore radioactive material like Thorium needs to be separated as well.

The major exporter in the world is the country China, where the needed environmental precautions are not fulfilled. The toxic waste in form of sludge is often just drained in big mud tanks under open sky. Thereby the chemicals and acids get into to groundwater affecting the entire region surrounding the mine. Following the groundwater cannot be used anymore for farming. Studies in the field of the mining of rare earth material show high cancer risks for the labors that are directly involved in the preparation of the rare earth materials.

The prices for rare earth materials have dropped for the past 5 years, whereby these became more popular for electrical applications. However this low price can only be sustained by the poor labor conditions and the disregard of toxic waste treatment. From an ethical and sustainable perspective these factors need to be taken into account as well. Hereby the question arouses: Do the technical advantages using rare earth materials in electrical devices outweigh the ecological and social damage caused by the mining?

[15]

# Bibliography

- [1] Fredrik Hedenus, Martin Persson, and Frances Sprei, *Sustainable development. history, denition & the role of the engineer*. 2015.
- [2] Daniel Pehrman and Mathias Jones, “Start capability of industrial synchronous motor with high efficiency”, Master’s Thesis in Electric Power Engineering, Chalmers University of Technology, Göteborg, 2014.
- [3] European Parliament, *Commission regulation (ec) no 640/2009*, 22 July 2009.
- [4] European Parliament, *Commission regulation (eu) no 4/2014*, 6 January 2014.
- [5] Reza Rajabi Moghaddam, “Synchronous reluctance machine (synrm) in variable speed drives (vsd) applications”, PhD Thesis, The Royal Institute of Technology, KTH, Stockholm, May 2011.
- [6] J.M. Stephenson and P.J. Lawrenson, “Average synchronous torque of synchronous machines, with particular reference to reluctance machines”, Proc. IEE Vol. 116, No 1969 June, University of Leeds, Leeds, December 1968.
- [7] M. Gamba, G. Pellegrino, A. Vagati, and F. Villata, “Design of a line-start synchronous reluctance motor”, Electrical Machines & Drives Conference (IEMDC), 2013 IEEE International, 2013.
- [8] Harold L. Garbarino: Eric T.B. Gross, “The georges phenomenon - induction motors with unbalanced rotor impedances”, AIEE Transactions Rotating Machinery, Illinois Institute of Technology, Chicago, August 1950.
- [9] P.J. Lawrenson and M. Mathur, “Pull-in criterion for reluctance motors”, Proc. IEE, Vol.120, No 9, September 1973, University of Leeds, Leeds, January 1969.
- [10] Sheikh F. Rabbi and M. Azizur Rahman, “Critical criteria for successful synchronization of line start-ipm motors”, IEEE Journal of emerging and selected topics in power electronics ,Vol. 2, No 2, June 2014, pp.348-358, University of Newfoundland, St. Johns, December 2013.
- [11] *Estimation of pump moment of inertia – neutrium*, 2013. [Online]. Available: <https://neutrium.net/equipment/estimation-of-pump-moment-of-inertia/> (visited on 05/01/2017).
- [12] CIRCUTOR, *Slot harmonics in power generation systems*. [Online]. Available: <http://circutor.com/en/documentation/articles/3119-slot-harmonics-in-power-generation-systems> (visited on 05/08/2017).

- [13] K.Bourchas, A.Stening, J. Soulard, A. Broddfalk, M. Lindenmo, M. Dahlén, F. Gyllensten, “Influence of cutting and welding on magnetic properties of electrical steel”, Electrical Machines (ICEM), 2016 XXII International Conference, 4.-7 September 2016.
- [14] Yujing Liu, Kashif S.K., Sohail A. M., “Engineering considerations on additional iron losses due to rotational fields and sheet cutting”, 18th International Conference on electrical Machines, 6-9 Sept. 2008.
- [15] ARD, *Schattenseite der windräder: Das schmutzige geheimnis sauberer windräder*, TV series Panorama, (broadcasted on 4/28/2011).